3.2 Antiproton Collection

3.2.1 Machine physics and potential

Potentially, antiproton collection and beam transport efficiency can be greatly improved between the antiproton production target and the Debuncher. An increase in the effective aperture due to better beam steering, an improved optics match and the removal of aperture restrictions would provide the largest contribution to increasing antiproton yield. These improvements should almost double the antiproton yield as compared with the historical best. A more modest gain of 10 to 20% is expected due to modifications to the lithium lens. Reducing the beam spot from its current size will also result in a 5 to 10% increase in antiproton yield. To accommodate increased beam power on the production target from slip stacking, a sweeping system will be installed. With the sweeping system, the beam spot size can remain small, even after slip stacking brings twice the proton beam intensity. Overall, the antiproton yield is expected to grow from the present level of 15×10^{-6} to about 40×10^{-6} antiprotons per proton after the collection and beam transport upgrades have been implemented.

We will start our consideration with the basic physics principles that determine antiproton production and collection. Then, we will consider practical limitations and formulate the upgrade path.

3.2.1.1 Optimization of production and collection for antiprotons created in the target

Currently, a nickel target is used for antiproton production. Nickel can sustain an unusually large energy deposition of up to 1000 Joules/g and is therefore considered to be the best material for the target.[19] Simulations of antiproton production in a nickel target were performed by with MARS code developed by N. Mokhov.[20] Figure 3.2.1 presents the total yield of antiprotons produced by a 120 GeV proton beam into a momentum acceptance of ±2.25% about an 8 GeV kinetic energy as a function of the target length. One can see that the total yield grows rapidly with target length, but unfortunately the phase space density is saturated well before the total antiproton yield is maximized. In reality, only a small fraction of antiprotons are accepted into the debuncher and one needs to find an optimum set of conditions to fit the maximum number of antiprotons into the finite phase space of the ring. Figure 3.2.2 shows the coordinates of antiprotons in the $x - x'$ phase space produced by a proton beam with rms beam size of 100 µm and an 8 cm long nickel target. Particle x-coordinates were translated to the longitudinal coordinate at which the second order moments $\langle x\theta_x \rangle$ and $\langle y\theta_y \rangle$ are equal to zero. If there were no scattering or absorption of antiprotons in the target, this coordinate (waist position) would be in the center of the target. In reality, it is shifted downstream of the target center. We denote this position by δs. For an 8 cm target, it is approximately 2.1 mm. The circle on the plot presents the boundary of phase space with acceptance $\varepsilon = 25$ mm mrad and β function $\beta^* = 1.5$ cm.
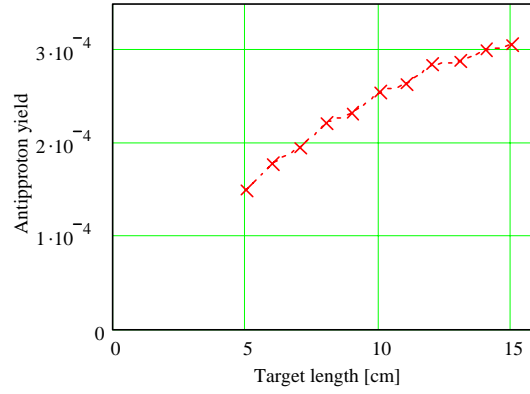
Figure 3.2.1 Dependence of total antiproton yield on the length of the nickel target for a 120 GeV proton beam, momentum acceptance is ±2.25%.
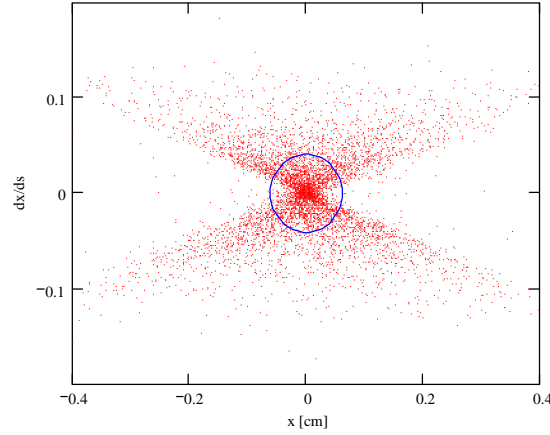

Figure 3.2.2 *Coordinates of antiprotons in x - x′ phase space simulated with MARS code for a proton beam of 120 GeV and an rms beam size of 100 μm. The circle inscribes a phase space with ε = 25 mm mrad and β* = 1.5 cm.*

Figure 3.2.3 shows the angular distribution function for antiprotons exiting the target. As one can see from the figure, it can be described by a gaussian distribution[21]

$$f(\theta) \propto \exp\left(-\frac{\theta^2}{2\sigma_\theta^{\,2}}\right)$$

$$\sigma_\theta \approx \frac{1.1}{\gamma}\sqrt{\frac{m_\pi}{m_p}}$$

(3.2.1)

where m_p and m_π are the proton and pion masses, σ_θ=45 mrad.

Figure 3.2.4 shows the antiproton yield as function of β^* for different target lengths and machine acceptances. Horizontal and vertical acceptances are considered to be equal; and the momentum acceptance is ±2.25%, so that the phase space of the accepted antiprotons is determined by the following equations,

$$\left(\frac{x_i^{\,2}}{\beta^*} + x_i'^2\beta^*\right) + \left(\frac{y_i^{\,2}}{\beta^*} + y_i'^2\beta^*\right) \le \varepsilon$$

$$\left|\frac{\Delta p_i}{p_0}\right| \le 0.0225$$

(3.2.2)

The β functions are related to the waist position, δs, whose dependence on target length is presented in Figure 3.2.5. The waist is displaced from the target center due to scattering and absorption of antiprotons in the target.
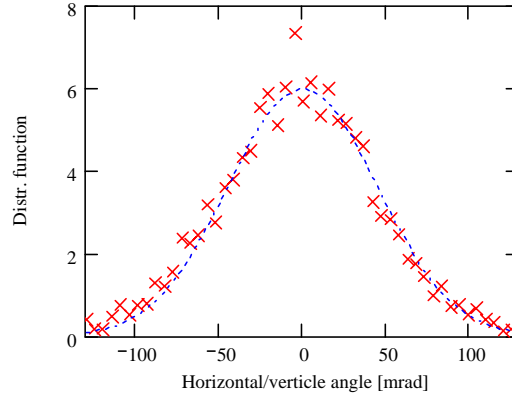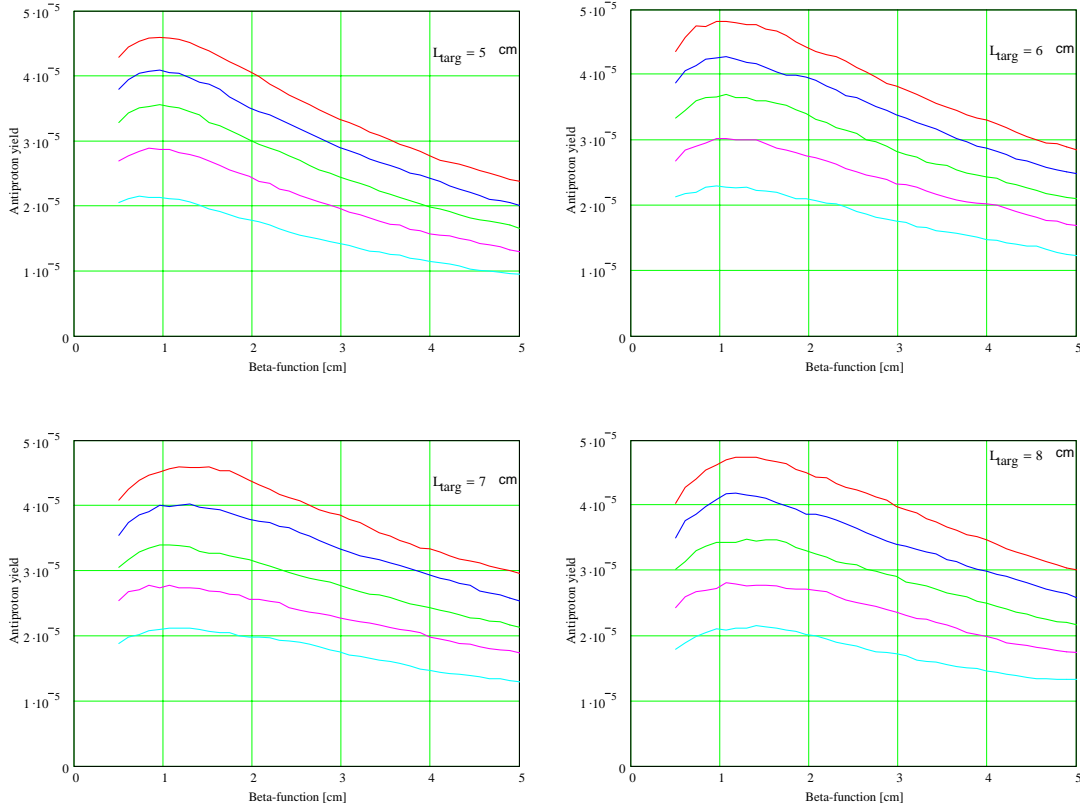

Figure 3.2.3 *Angular distribution function of 8 GeV antiprotons coming out of an 8 cm nickel target; proton beam energy is 120 GeV. The dashed line represents a gaussian distribution with* $\sigma_\theta = 45$ *mrad*
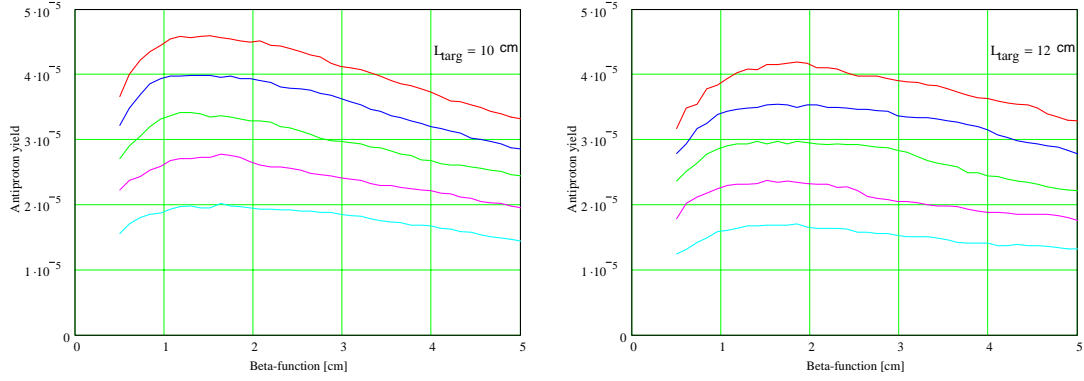
Figure 3.2.4 *Dependence of antiproton yield into ±2.25% momentum spread on the β function at the target for the beam acceptances of 15, 20, 25, 30 and 35 mm mrad, and target lengths from 5 to 12 cm. Corresponding waist positions are shown in* Figure 3.2.5. *The proton beam energy is 120 GeV, and the rms beam size at the target is 100 μm. The kinetic energy of antiprotons is 8 GeV.*

As one can see from Figure 3.2.4, for every given target length, the maximum yield is achieved at an optimal β function which is almost independent of acceptance. Figure 3.2.6 shows the maximum antiproton yield as function of the target length for different machine acceptances and for the optimal β function. Figure 3.2.7 shows the dependence of this optimal β function on the target length. The optimal β function is approximately 1/6 of the target length, which is significantly different from the $1/2\sqrt{3}$ dependence predicted in reference [21]. Taking this into account, we can introduce the effective emittance of antiprotons exiting the target to be equal to

$$\varepsilon_{eff} \equiv \beta^*_{opt}\sigma_\theta^{\,2} \approx \frac{1}{5}\frac{m_\pi}{m_p}\frac{L_{t\,\mathrm{arg}}}{\gamma^2}$$

(3.2.3)

where $\beta^*_{opt} = L_{t\,\mathrm{arg}}/6$ is the optimal β function, and L_{targ} is the target length. For a target length of 8 cm, that yields $\varepsilon_{eff} \approx 26$ mm mrad.
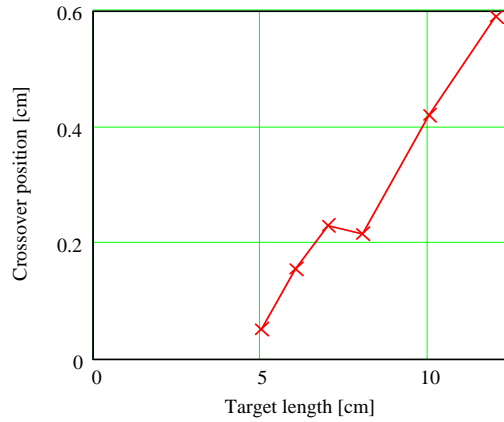

Figure 3.2.5 *Dependence of the waist position on the target length for data presented in Figure 3.2.4; proton beam energy is 120 GeV, and rms beam size at the target is 100 μm.*

61

In the above discussion, the antiproton yield was calculated for an ideal but unfortunately non-realistic collection scheme. Large antiproton angles require a short focusing lens for their collection. The lithium lens is the most appropriate focusing element for the Fermilab antiproton source parameters, but scattering and absorption in the lens as well as its non-linearity cause a reduction in antiproton yield. There are also practical limitations on the achievable lithium lens focusing strength, which further complicate the optimization. We consider this in detail in the following sections.
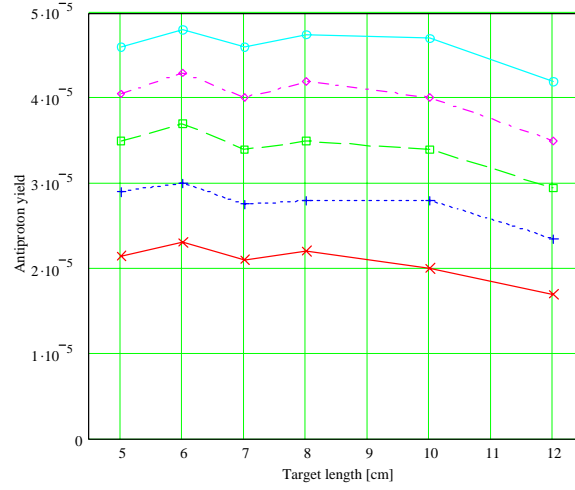
Figure 3.2.6 *Dependence of maximum antiproton yield into ±2.25% momentum spread on the target length for the beam acceptances of 15, 20, 25, 30 and 35 mm mrad. Proton beam energy is 120 GeV, and rms beam size at the target is 100 μm. Kinetic energy of antiprotons is 8 GeV.*
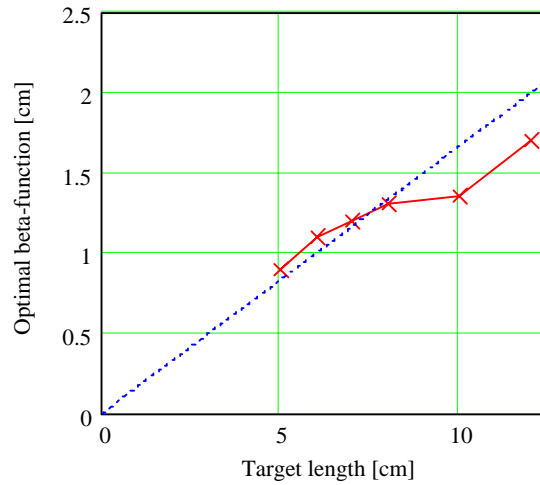
Figure 3.2.7 *Dependence of the optimal β function on the target length for data presented in Figure 3.2.6.*

3.2.1.2 Scattering and absorption of antiprotons in the lithium lens

Nuclear scattering and absorption of the antiprotons in the lithium lens are the major mechanisms for antiproton loss in the lens. The loss of antiprotons due to their strong interactions with lens material can be estimated by the following expression,

$$\kappa_{lens} = \exp\left(-\frac{L_{Li}}{L_{Abs_{Li}}} - \frac{L_{Be}}{L_{Abs_{Be}}}\right) \approx 0.82$$

$$(3.2.4)$$

where L_{Li} =15.5 cm and L_{Be}=1.2 cm are total lengths of lithium and beryllium traversed by the beam, and $L_{Abs_{Li}}$ =102 cm and $L_{Abs_{Be}}$ =30.2 cm are nuclear collision lengths for lithium and beryllium. This estimate is in remarkable agreement with the results from MARS simulations.

Multiple scattering in the lens can be estimated by the following formula,

$$\sqrt{\overline{\theta^2}} = \frac{13.6\,\text{MeV}}{\beta Pc}\sqrt{\frac{L_{Li}}{X_{Li}} + \frac{L_{Be}}{X_{Be}}}$$
$$= 0.635\,\text{mrad}$$

$$(3.2.5)$$

where X_{Li}=155 cm and X_{Be}=35.3 cm are the radiation lengths for lithium and beryllium. Figure 3.2.8 presents a comparison of results obtained with Eq.(3.2.5) and the results from MARS simulations. There is good agreement between simulation and Eq.(3.2.5) for angles below 2 mrad. For large angles, as is expected, MARS produces long non-gaussian tails. Only a small fraction of the particles are located in the tails, therefore we can neglect them with a negligible penalty in the accuracy of the calculations. The scattering in the lens causes emittance growth, which can be estimated by the following formula:

$$\Delta\varepsilon = R_{lens}\sqrt{\overline{\theta^2}}$$

$$(3.2.6)$$

For a lens with radius 1 cm, that yields $\Delta\varepsilon$ = 6.3 mm mrad. Figure 3.2.9 shows the decrease in antiproton yield due to multiple scattering in the lens for a fixed β function at the target of 1.5 cm. One can see that for acceptances above 20 mm mrad, the loss is sufficiently small so that nuclear absorption is the major mechanism for particle loss. For smaller acceptances, multiple scattering causes a significant loss in yield. This can be partially compensated for by reducing the β function on the target as shown in Figure 3.2.10.
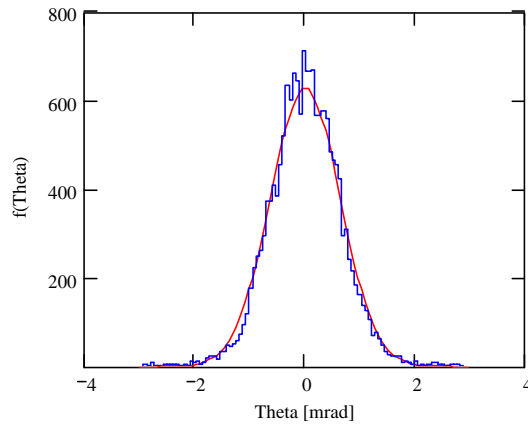

Figure 3.2.8 *Distribution functions of a point like beam after passing through the lithium lens, simulated by MARS and computed with use of the multiple scattering formula of Eq. (3.2.5).*
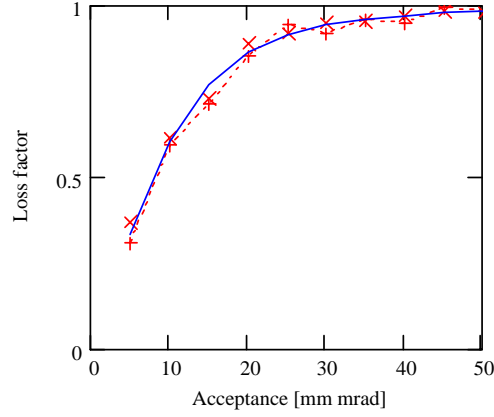
Figure 3.2.9 *Loss of antiproton yield due to multiple scattering as a function of machine acceptance for the current lithium lens. The β function at the target is 1.5 cm.*
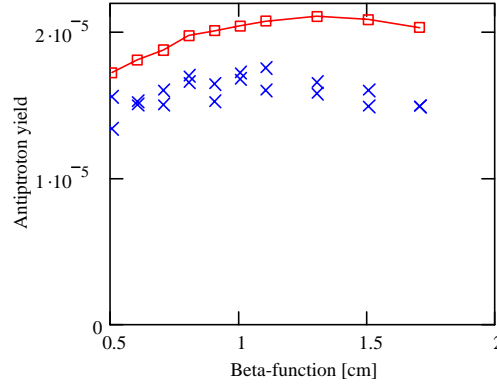
Figure 3.2.10 *Dependence of antiproton yield on the beta function at the target for an acceptance of 15 mm mrad. Solid line – no scattering and absorption in the lens, $\times$ – only multiple scattering is taken into account.*

To optimize the antiproton yield with multiple scattering taken into account, we assume that the phase space of antiprotons accepted into the ring is described by the following expression,

$$\frac{x_i^{\,2} + y_i^{\,2}}{R_{lens}^{\,2}} + \frac{x_i'^{\,2} + y_i'^{\,2}}{\varepsilon^2} R_{lens}^{\,2} \leq 1$$

$$\left| \frac{\Delta p_i}{p_0} \right| \leq 0.0225$$

(3.2.7)

That means that the accepted antiprotons take up the entire lens cross-section and the β function at the exit of the lens has zero derivative. Figure 3.2.11 presents the antiproton yield as function of lens gradient for different lens lengths and radii. Multiple scattering is taken into account, but the lens is still considered to be linear. As will be shown below the non-linearity does not affect the yield for current lens parameters. For every given lens gradient, the distance between the lens and the target was adjusted to achieve the maximum yield.
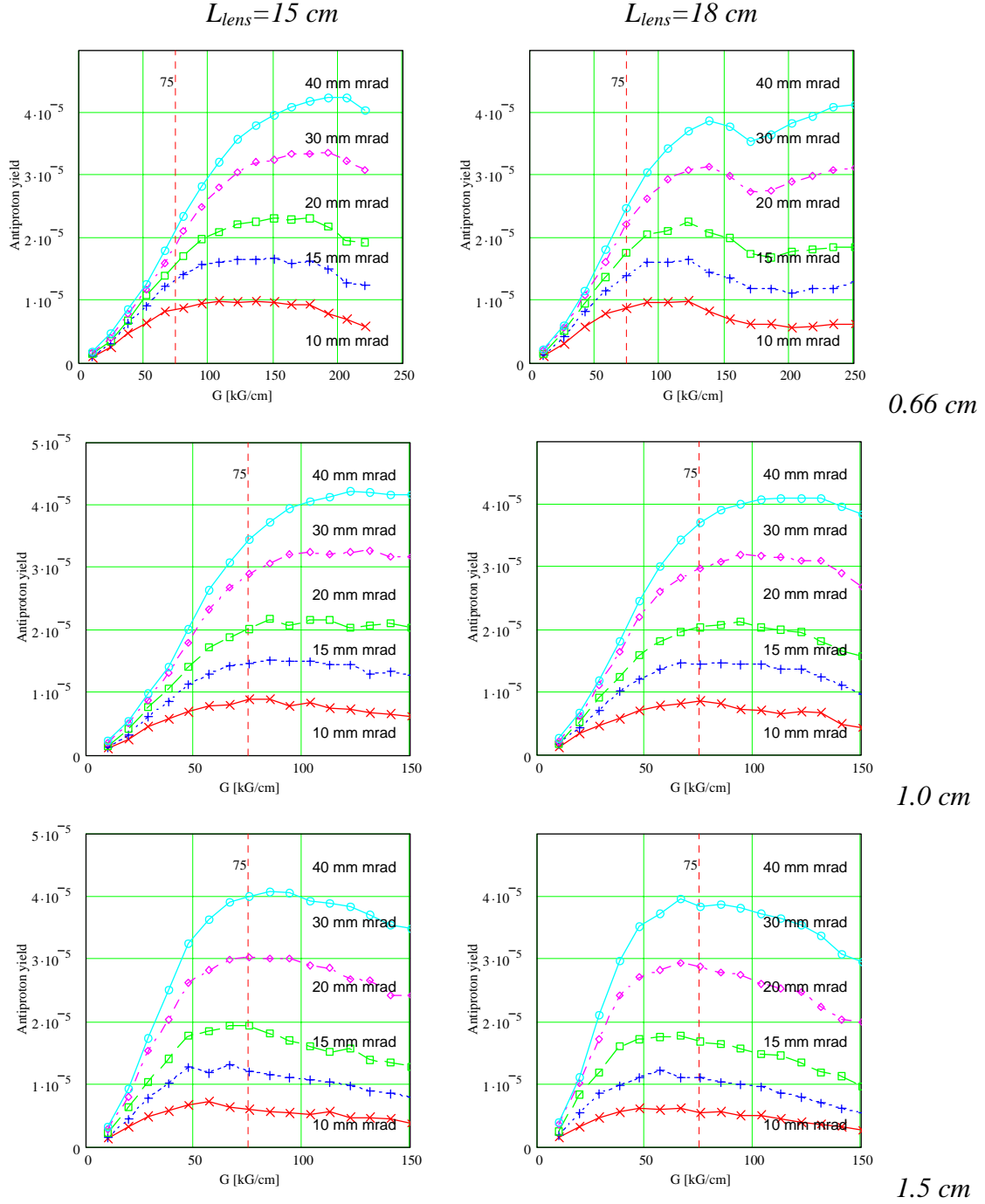
Figure 3.2.11 *The dependence of antiproton yield on the lithium lens gradient for different lens lengths and radii; top - $R_{lens}=0.66$ cm, middle - $R_{lens}=1.0$ cm, bottom - $R_{lens}=1.5$ cm. Rms proton beam size at the target is 130 μm. Energy acceptance is $\pm2.25\%$.*

One can see that the peak yield is decreasing with increased radius and length of the lens. The former occurs due to a larger contribution of multiple scattering (see Eq.(3.2.6)), while the latter is related to increased antiproton absorption. The current design of the lithium lens limits its gradient to about 75 kG/cm. Up to this maximum gradient, all

measurements of antiproton collection have exhibited an antiproton yield growth with increasing lens strength. That agrees with simulations, but one should not expect that a further increase of the focusing would bring a significant improvement for acceptances below 20 mm mrad. There can be a moderate increase for larger acceptances, but even in the case of 40 mm mrad acceptance, a yield increase of about 20% would require a 50% increase in lens gradient. That is not possible with a lens of the current design. Note that although reducing the lens radius looks like a reasonable alternative based on Figure 3.2.11, it is limited by rapid growth of the beam size downstream of the lithium lens. A lens radius around 1 cm is about the minimum that can be used to match the lens to the downstream optics (see section 3.2.1.5 for a description of the AP2/Debuncher aperture improvements).

3.2.1.3 Target energy deposition and beam sweeping

Antiprotons are produced from the interaction between a 120 GeV proton beam from the Main Injector and a nickel target. Quadrupole magnets focus the incident beam on the target, a smaller beam spot increases the antiproton collection efficiency, but also increases the peak energy deposition on the target. Early targets made of Tungsten were damaged at only modest intensities, so a switch to copper targets was made in the late 1980's. When intensities in the old Main Ring reached their peak at around 3.25×10^{12} protons per pulse (ppp), measurements indicated that melting occurred during the beam pulse and adversely affected the yield. Though the reduction in yield from melting was only a few percent, it became clear that a change in target material, spot size or beam position would be required for running at intensities expected in the Main Injector era without a significant reduction in yield. The penalty for increasing the energy deposition beyond the melting point would not only be reduced yield, but possible damage due to the shock waves developed in the target during the beam pulse.

During the latter part of Collider Run I, nickel targets began to be used in place of the copper targets. Nickel is similar in atomic structure to copper, so the optimum target length and yield characteristics of the two materials are nearly identical. Nickel has the advantage that the onset of melting requires nearly twice the energy deposition as copper. In addition, nickel is more tolerant of the shock waves that will develop during the beam pulse. However, without a beam sweeping mechanism in place, the spot size on the target would still need to be increased to prevent damage.

Figure 3.2.12 illustrates the dependence of antiproton yield on the targeted rms proton beam size for different acceptances and a lens gradient of 75 kG/cm. One can see that the antiproton yield begins to decrease for beam sizes greater than 100 μm and that the rate of decrease is faster for smaller acceptances. To maximize antiproton yield, it would be desirable to keep the proton beam size at or below 100 μm. The transport line leading to the target is capable of delivering a beam spot size that is this small. However, reducing the beam to this size with a proton intensity of 5×10^{12} ppp would result in a peak energy deposition in the target beyond the melting point of nickel. Figure 3.2.13 shows the relationship between beam spot size, antiproton yield and peak energy deposition with 5×10^{12} protons on target. Melting in the nickel target would be expected with spot sizes below about 0.2 mm. Under these conditions, the ideal spot size to produce maximum yield would most likely cause damage to the target. Slip stacking in

the Main Injector could bring as much as 1×10^{13} protons on target, further aggravating the problem.

Note that over the range of possible antiproton source parameters, the following empirical formula can be used to closely approximate the results of numerical calculations[22]

$$E_D \approx 890[\text{J/g}]\left(\frac{200\,\mu\text{m}}{\sigma_{pb}}\right)^2 \frac{N_p}{5\cdot10^{12}}$$

(3.2.8)

The formula determines the peak energy deposition as a function of the rms size of the proton beam, σ_{pb}, and the number of protons on target, N_p. Note also that the development of the particle shower causes the peak energy deposition to be about twice the energy deposition due to ionization losses of the primary proton beam.
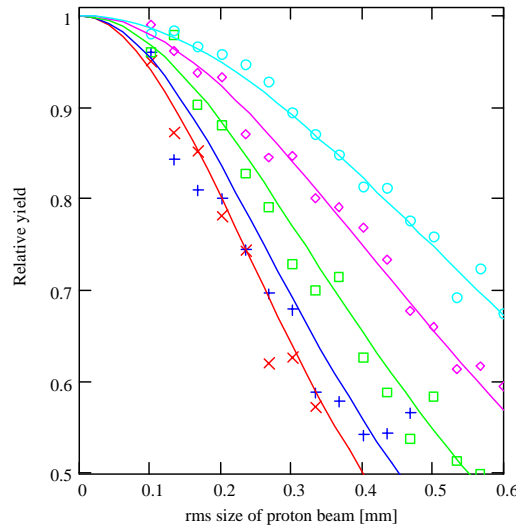
Figure 3.2.12 *Dependence of relative antiproton yield on rms size of the proton beam for acceptances of 10, 15, 20, 30 and 40 mm mrad (curves follow from bottom to top); target length of 8 cm, antiproton absorption and scattering in the lens are taken into account, lens gradient is 75 kG/cm.*

The idea of sweeping the proton beam across the target to reduce peak heating is not a new one, the Tevatron I design report included beam sweeping as a future upgrade. The design phase of the sweeping project began in 1993 and included several years of research and development. Early sweeping designs made use of kicker style magnets similar to those used to transfer beam between the accelerators. In the final design, the sweeping magnets have four two-phase conductor windings rotated about the beam axis to correct magnetic field non-linearities. The proton beam traces a circular trajectory about the target during the beam pulse as illustrated in Figure 3.2.14. The power supply required to provide the bipolar magnet current pulse involves two-stage compression with saturated reactors.

The targeted beam needs to be moved about 0.3 mm during the 1.6 μs beam pulse, resulting in about a factor of five decrease in the peak energy deposition. This reduction is enough so that the spot size can be reduced almost to the point that maximum

yield can be attained, even after slip stacking is commissioned. Sweeping magnets are required both upstream and downstream of the target to preserve the proper trajectory of the antiprotons entering the AP-2 line. There is a small loss of aperture due to the larger beam size passing through the lithium lens. The sweep magnets are of a single design, there are two upstream sweep magnets and a single downstream sweep magnet because the proton beam has an energy of 120 GeV and the antiproton beam is only 8 GeV. There are differences in the striplines and other external details of the downstream magnet in the vault as compared to the upstream magnets located in the AP-1 line.
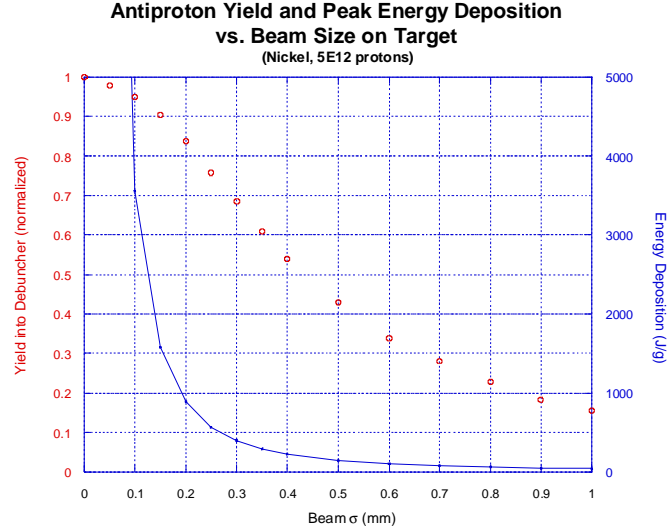

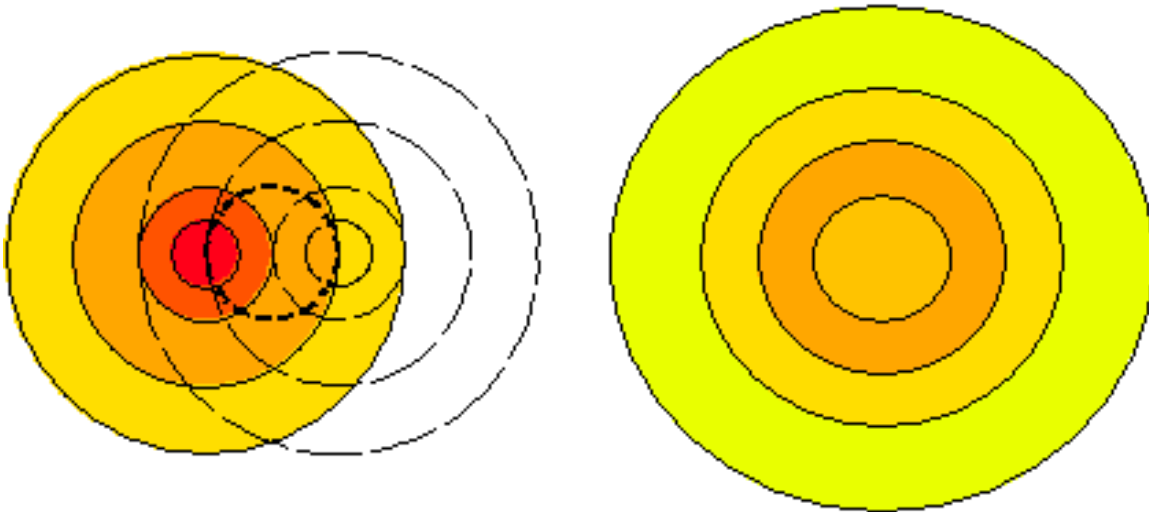Figure 3.2.13 *Beam spot size vs. Debuncher yield and peak energy deposition in the target (15 mm mr).*

Figure 3.2.14 *Reduction in peak energy deposition with beam sweeping*

3.2.1.4 Effects of lithium lens focusing non-linearity on the antiproton yield

A major non-linearity in the lithium lens focusing is related to the skin effect. At present, the lens current represents a 350 μs long half-period sinusoidal pulse. The skin depth at the characteristic frequency $1/(2*0.00035) \approx 1400$ Hz is 4.5 mm. That is half the size of the lens radius and implies that there is a significant delay in the penetration of magnetic field in to the lens. Figure 3.2.15 shows the results of calculations of the magnetic field penetration into a lithium cylinder with 1 cm radius. It was obtained by expanding the pulse into a Fourier series, finding the solution for the harmonics and performing an inverse Fourier transform numerically. One can see that the maximum gradient is achieved at an RF phases between 30 and 60 deg. There is also a solution for a continuous sinusoidal wave shown in the figure. Although this solution is quite different at the beginning of the pulse, it converges later and there is a negligible difference for the 30 to 60 deg. phases of interest. Therefore we will use this solution,

$$B(r,t) = \frac{2I_0}{cr_0} \mathrm{Re}\left(\frac{\mathrm{ber}_1\left(\sqrt{2}\,r/\delta\right) + i\,\mathrm{bei}_1\left(\sqrt{2}\,r/\delta\right)}{\mathrm{ber}_1\left(\sqrt{2}\,r_0/\delta\right) + i\,\mathrm{bei}_1\left(\sqrt{2}\,r_0/\delta\right)} e^{i\omega t} \right)$$

(3.2.9)

for further calculations. Here δ is the skin-depth for frequency $f = 1/(2T)$, T is the duration of the pulse, I_0 is the current amplitude, r_0 is the radius of the lithium cylinder, and ber(x) and bei(x) are the modified Bessel functions. Expanding the Bessel functions into a Fourier series:

$$\mathrm{ber}_1(\mathrm{x}) \approx f_r(\mathrm{x}) \equiv \frac{1}{\sqrt{2}}\left(-\frac{\mathrm{x}}{2} - \frac{\mathrm{x}^3}{16} + \frac{\mathrm{x}^5}{384} + \frac{\mathrm{x}^7}{18432} - \frac{\mathrm{x}^9}{1474560} \right)$$

$$\mathrm{bei}_1(\mathrm{x}) \approx f_i(\mathrm{x}) \equiv \frac{1}{\sqrt{2}}\left(\frac{\mathrm{x}}{2} - \frac{\mathrm{x}^3}{16} - \frac{\mathrm{x}^5}{384} + \frac{\mathrm{x}^7}{18432} + \frac{\mathrm{x}^9}{1474560} \right)$$

(3.2.10)

we obtain an expression which has been used in the tracking simulations presented in Section 3.2.1.5,

$$B(r,t) = \frac{2I_0}{cr_0} \frac{\left(\dfrac{x}{2} - \dfrac{x^5}{384} + \dfrac{x^9}{147456} \right)\cos\tilde{\psi} - \left(\dfrac{x^3}{16} - \dfrac{x^7}{18432} \right)\sin\tilde{\psi}}{\sqrt{f_r^2(x_0) + f_r^2(x_0)}}$$

(3.2.11)

where

$$\tilde{\psi} = \omega t - \psi \quad , \quad \psi = \mathrm{atan}\left(\frac{f_i(x_0)}{f_r(x_0)} \right) + \frac{\pi}{4} \quad , \quad x = \sqrt{2}\frac{r}{\delta} \quad , \quad x_0 = \sqrt{2}\frac{r_0}{\delta}$$

(3.2.12)

Operationally, the present Fermilab lithium lens has a phase of $\psi = 30°$, a time when the magnetic field is still very nonlinear. Maximum linearity of the gradient is achieved at about 45° and the maximum magnetic field gradient is developed in the

center of the lens is at about 67° as shown in Figure 3.2.16. Gradient variations across the lens cross-section are ±7% at the phase of maximum linearity. The mean value of the gradient is about 77% of the gradient calculated without the skin-effect taken into account.
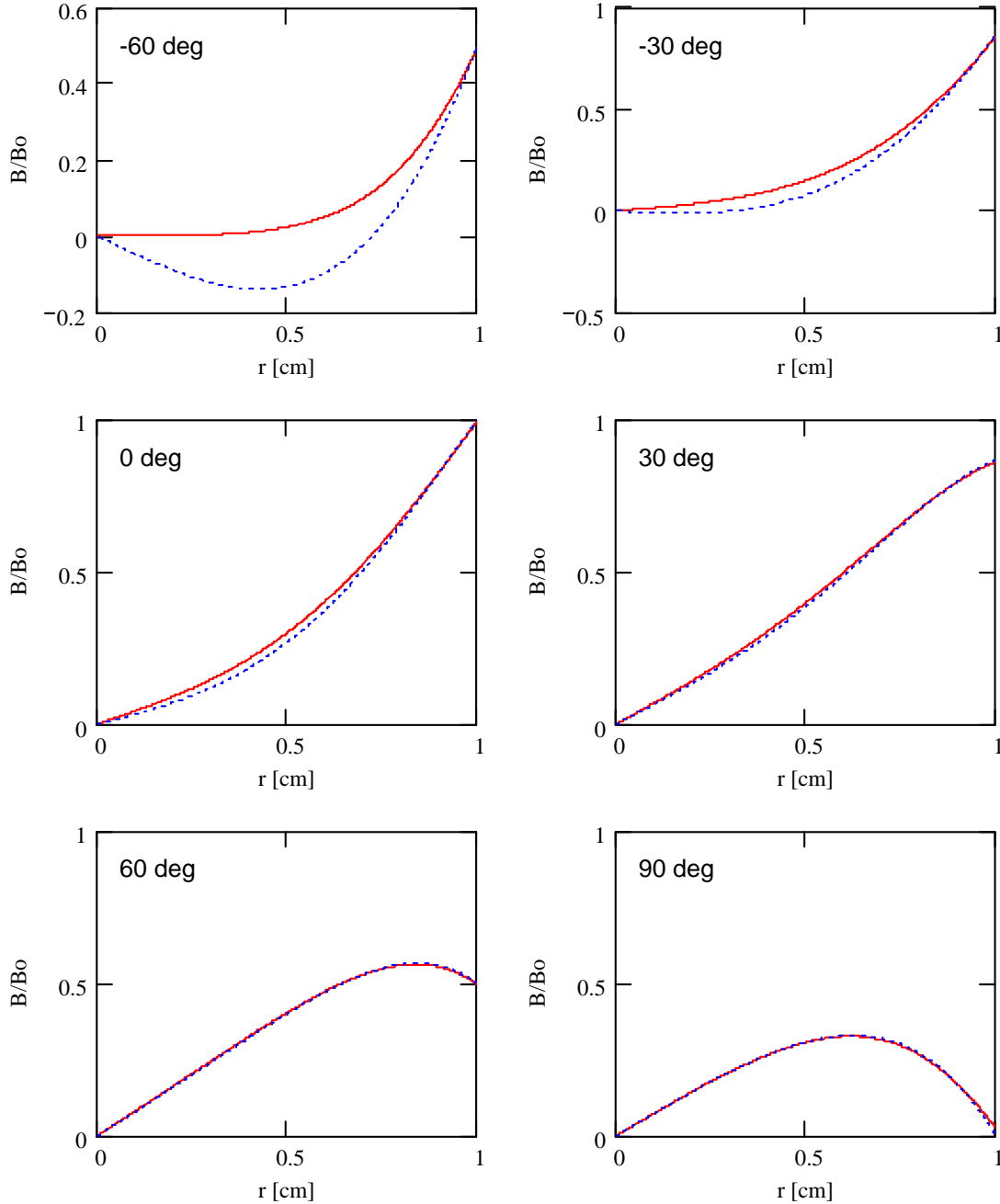

Figure 3.2.15 *Calculated dependence of the lens magnetic field on radius for different times during the 350 μs half period sinusoidal pulse. Time is expressed in phase so that the end and the beginning of the pulse correspond to ±90 deg. The dotted line represents the solution for a continuous sinusoidal wave.*

The temperature gradient across the lithium cylinder causes an additional non-linearity in the lens focusing. The gradient is related to the heating of the lens by the amplitude of the current pulse. For a 1.5 s repetition time, the average power left in the lens is about 100 W/cm. It produces a temperature gradient across the lens so that the exterior has a lower temperature and, consequently, lower resistivity. It produces higher current density in the exterior, which partially compensates for the magnetic field non-linearity due to the skin effect.

A worst-case estimate can be done for a stationary case. Then, the temperature dependence on radius is:

$$T(r) = T(0) + \frac{P}{4\pi\kappa} \frac{r^2}{r_0^2}$$

(3.2.13)

where $\kappa = 0.82$ W/cm/K is the thermal conductivity of lithium, and P is power per unit length. For $P = 110$ W/cm one obtain the temperature difference of 10 K and the corresponding current density change, $\Delta j/j$, of about 4%. That yields 2% correction for magnetic field with dependence on radius described by the following formula:

$$B(r) = B_0 \frac{r}{r_0} \left(1 + \frac{1}{2} \frac{\Delta j}{j} \frac{r^2}{r_0^2} \right)$$

(3.2.14)

In reality the time between pulses is longer than the decay time of the temperature wave,

$$\tau_Q = \frac{Cr_0^2}{2\kappa} \approx 1.2\,\text{s}$$

(3.2.15)

where $C = 1.95$ J/K/cm^3 is the heat capacity of lithium. That determines that the actual temperature difference is well below the above estimate.
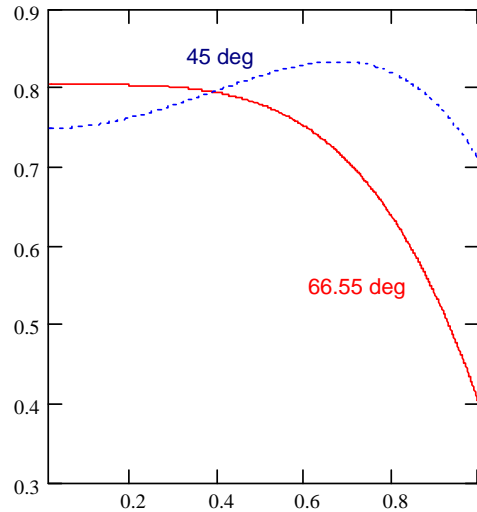

Figure 3.2.16 *Calculated dependence of lens magnetic field on radius at the time when the maximum linearity of focusing (45 deg) and the maximum gradient (66.55 deg) in the lens center are achieved. The result is normalized by the constant determined by the following equation:* $G_{max} = 2I_0 / cr_0^2$.

Non-linearities due to the lens edges are even smaller than those due to temperature gradient. For the stationary case in the lens body we can expand the current density from the lens axis,

$$j_z(r,z) = j_z(z)\big|_{r=0} - \frac{r^2}{4}\frac{d^2}{dz^2}\left(j_z(z)\big|_{r=0}\right) + \frac{r^4}{64}\frac{d^4}{dz^4}\left(j_z(z)\big|_{r=0}\right) + \ldots$$

(3.2.16)

That yields the following expansion for magnetic field,

$$B_\theta(r,z) = \frac{2\pi}{c}\left[rj_z(z)\big|_{r=0} - \frac{r^3}{8}\frac{d^2}{dz^2}\left(j_z(z)\big|_{r=0}\right) + \frac{r^5}{192}\frac{d^4}{dz^4}\left(j_z(z)\big|_{r=0}\right)\right] + \ldots$$

(3.2.17)

Integrating it with the equation of motion, one obtains the first non-linear correction for the lens focusing:

$$\frac{\Delta\Phi}{\Phi} = \frac{3}{8}\frac{rr'}{L_{lens}}$$

(3.2.18)

For $r = 1$ cm, $L_{lens}=15$ cm and $r' = 1/15$ we obtain $\Delta\Phi/\Phi\sim10^{-3}$. There is an additional correction related to sphericity of beryllium windows. Numerical solution for the stationary current contribution yields that this correction is about 3×10^{-3}.

Summarizing, we can conclude that the non-linearity due to the skin effect makes the largest contribution. We will neglect other non-linearities in further calculations. As was already mentioned, maximum lens linearity is achieved at 45 deg and this phase should be used for estimates in approximating linear focusing. Then for the lens gradient we can write

$$G \approx \frac{2I_0}{cr_0^2}\frac{\rho_{Ti}}{\rho_{Ti} + 2\rho_{Li}\frac{d_{Ti}}{r_0}}0.78 \approx \frac{2I_0}{cr_0^2}0.74$$

(3.2.19)

where $\rho_{Li} = 11.4\cdot10^{-6}$ $\Omega\cdot$cm and $\rho_{Ti} = 42\cdot10^{-6}$ $\Omega\cdot$cm are the resistivities for lithium and titanium, d_{Ti} is the thickness of titanium cylinder containing lithium, and the coefficient 0.78 is determined by the field decrease due to skin effect as was presented in Figure 3.2.16. Thus, the lens current of 500 kA corresponds to about 74 kG/cm lens gradient.

Simulations of the antiproton yield with the lithium lens non-linearity taken into account did not exhibit any significant drop in yield in comparison with the linear lens simulations. Figure 3.2.17 shows the change in yield as a function of the change of lithium lens strength and the proton beam arrival time expressed in the phase of the lens pulse for two different pulse lengths. One can see that shortening the lens pulse from 360 to 200 μs reduced the yield by only about 2% while the non-linearity, $B(r)/r$, grew from ±7% to (+10 − -50)%. Figure 3.2.17 also depicts that due to the stronger skin effect for a shorter pulse, one needs to change the arrival time from 40 to 75 deg. and to increase the lens current by 1.8/1.3~1.4 times to compensate the gradient loss. Thus, a decrease of the lens power consumption due to shorter pulse is overcompensated by increased lens current and the total power consumption ends up being higher for a shorter pulse. Similarly, the power consumption grows for a pulse longer than 360 μs because in this

case the lens current is not changed significantly and power grows proportionally with pulse length. Thus, the choice of a 360 μs pulse length looks to be well optimized.
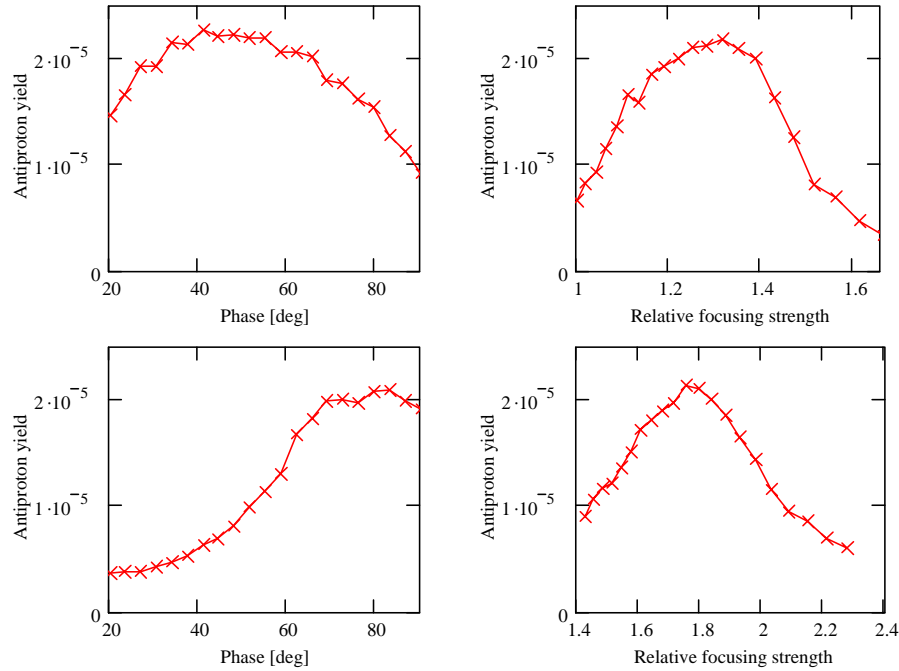

Figure 3.2.17 *Dependence of antiproton yield on the arrival time (left) and the lithium lens current (right) for a pulse lengths of 360 μs (top) and 200 μs (bottom). Arrival time is expressed in degrees of pulse phase. The focussing strength is given relative to the strength without the skin effect. Transverse acceptance is 20 mm mrad; the momentum acceptance is ±2.25%.*

3.2.1.5 Effects of the Debuncher acceptance on AP-2 line optics

In optimum conditions, the β function at the exit of the lens is determined by its radius and the acceptance of antiprotons captured in the Debuncher, $\beta_{lens} = r_0^{\;2} / \varepsilon$. That means that if the Debuncher acceptance is increased, the optics of the transport line has to be modified so that the target assembly optics will be matched with the Debuncher optics. Figure 3.2.18 presents β functions and dispersion functions optimized for Debuncher acceptances of 25 and 40 mm mrad. One can see that an increase in Debuncher acceptance decreases the β function in the lithium lens. Consequently, that leads to a β function increase in the first triplet, so that the beam size in the triplet grows proportionally with the acceptance of the Debuncher. There is plenty of free aperture in the first triplet for a 25 mm mrad acceptance, but it begins to get tight for a 40 mm mrad acceptance. Figure 3.2.19 presents the beam envelopes and aperture limitations for 25 and 40 mm mrad acceptances.

Another concern for the AP2 beam optics is the effects of energy spread on beam transport. The energy spread of protons accepted into the Debuncher is more than ±2% and one needs to identify how much it compromises beam transport quality. Figure 3.2.20 presents the results of particle tracking through the line. One can see that rms emittances decrease rapidly at the beginning of the line. That is related to scraping particles at the beam exterior and is accompanied by a reduction in beam intensity as can be seen from

the bottom portion of Figure 3.2.20. Note also that the scraping also causes step decreases in the beam envelopes (determined as the maximum particle transverse coordinate for a given longitudinal position). Through most of the line, the beam emittances do not grow. However, at the end of the line, there is a significant vertical emittance increase which is accompanied by an intensity decrease due to scraping at the very end. This emittance growth is related to chromatic effects, which are most pronounced at the end of the line due to the very strong focusing from the vertical dispersion suppressor quadrupoles.
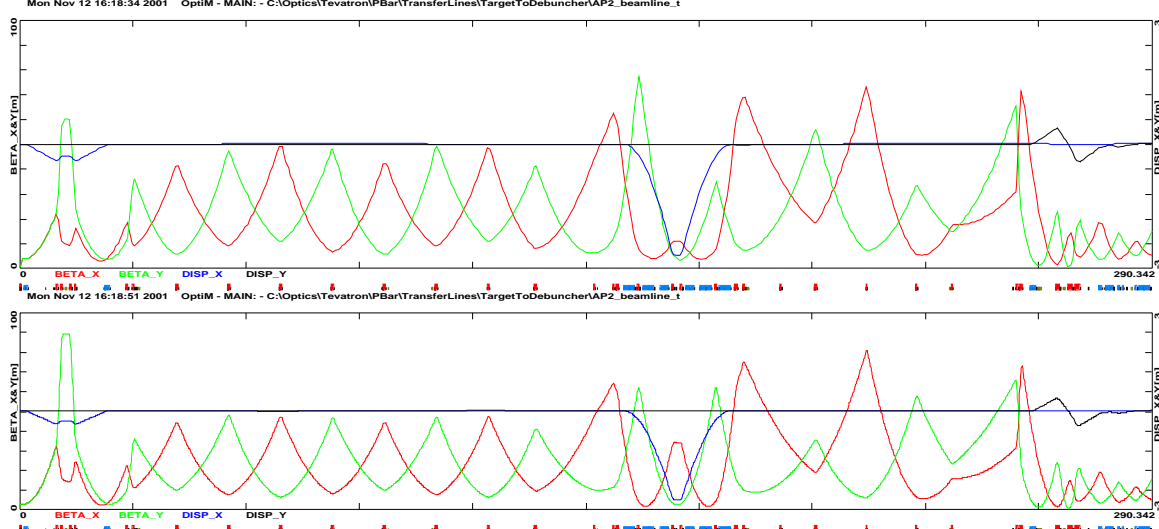
Figure 3.2.18 β functions and dispersion in the AP2 line for Debuncher acceptance of 25 mm mrad (top) and 40 mm mrad (bottom).

Figure 3.2.21 presents the dependence of antiproton yield on the acceptance at three different locations along the line and for two different optics solutions optimized for 25 and 40 mm mrad and a lithium lens gradient of 75 kG/cm. The chosen locations are (1) the target exit where the phase density is not disturbed by any optics effects, (2) the middle of the transport line before the main horizontal bends where the optics effects do not cause a phase space dilution, and (3) the end of the line. The dependence of yield on acceptance was obtained by particle tracking from the target to the chosen locations with all optics effects (including lens non-linearity and scattering) taken into account. To compute the yield, we counted the antiprotons that were able to pass through the AP-2 line and fell inside the Debuncher acceptance. As one can see, the transport through the first half of the line causes about a 30% decrease in the antiproton yield. It is related to the scattering and absorption of antiprotons in the lens. This is verified by good agreement between yields calculated by particle tracking through the first half of the line and computations presented in Figure 3.2.11 which takes into account only scattering and absorption in the lithium lens (shown by crosses in Figure 3.2.21). The tracking exhibited about 10% dilution in the second half of the line, which is related to chromaticity at the end of the line. One can also see that both optics exhibit approximately the same antiproton yield in the acceptance range of 10 to 40 mm mrad, which illustrates the relative insignificance of a "perfect" optics match in the AP-2 line. This occurs if the beamline acceptance is larger than the Debuncher acceptance.
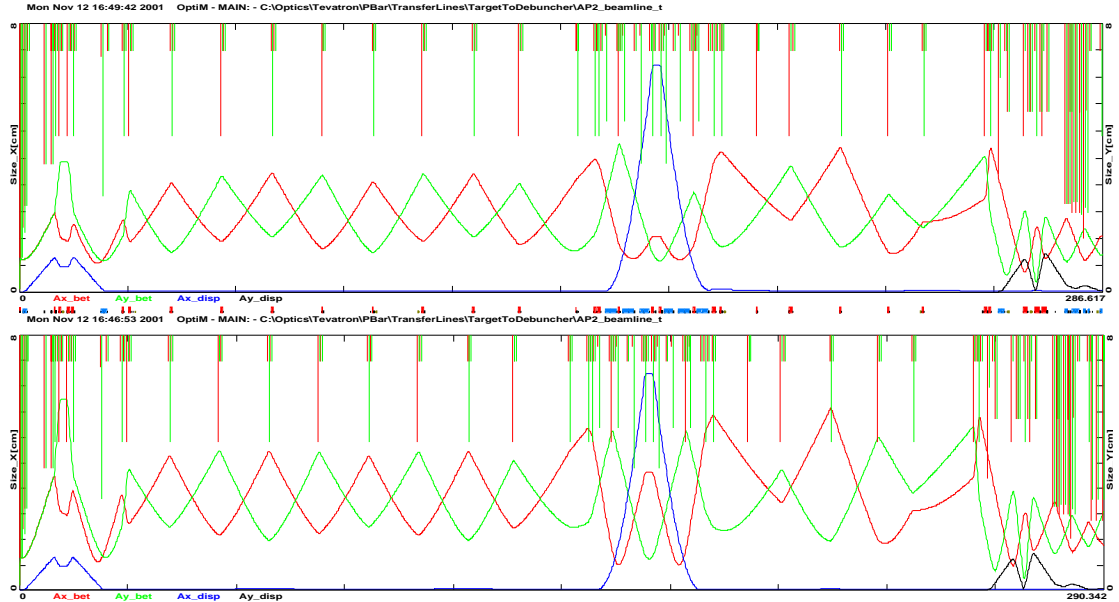
Figure 3.2.19 *Beam envelopes in AP2 line for a Debuncher acceptance of 25 mm mrad (top) and 40 mm mrad (bottom). Aperture limitations are shown by the vertical lines with the colors corresponding to the color of the same plane. Synchrotron size is shown for an energy spread of 2.5%.*
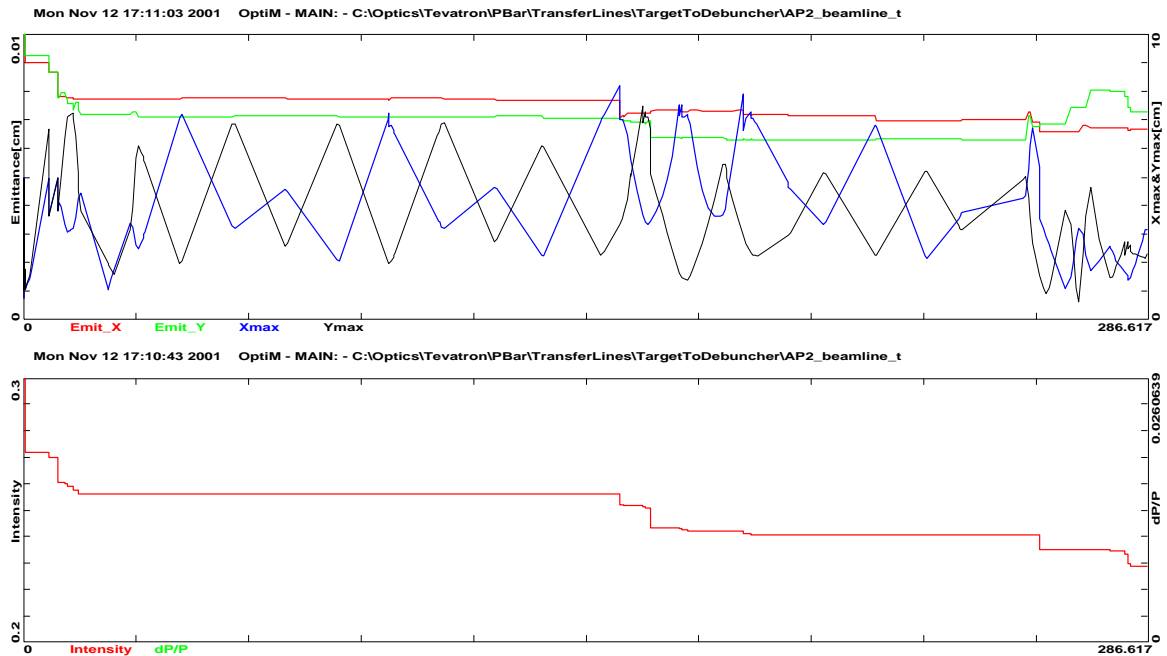
Figure 3.2.20 *Tracking results for optics optimized for 25 mm mrad acceptance. The top picture presents horizontal and vertical rms emittances for surviving particles and horizontal and vertical beam envelopes in the AP-2 line. The bottom picture depicts the antiproton intensity relative to the total antiproton yield from the target (fraction of surviving antiprotons).*

75

There are two types of chromaticity affecting the performance of the beamline. They are the chromaticity of the beam envelope and the chromaticity of dispersion. The major contribution for this emittance growth comes from the chromatic behavior of the vertical beam envelope. Figure 3.2.22 presents the ratio of the vertical β function for particles with a momentum offset to the vertical β function for particles at the nominal energy as a function of the vertical betatron phase advance. With these variables, the perturbation of the β function oscillates at double the betatron frequency. The initial β function oscillation is excited by the lithium lens with amplitude

$$\frac{\Delta\beta}{\beta} \approx \frac{F}{\beta^*} \frac{\Delta p}{p}$$

(3.2.20)

where β^* is the β function at the target, and F is the lithium lens focusing distance. That corresponds with $\Delta\beta / \beta \approx 0.2$ for a 2% momentum deviation. Then the β function is also excited in the first triplet and oscillates with approximately the same amplitude to the end of the line, where it is strongly excited by the strong quads of the vertical dispersion suppressor. The real problem is actually related to the second order correction for the beta function perturbation. To demonstrate it, the maximum β function oscillations are plotted as a function of momentum in Figure 3.2.23. To take into account that the phase of the perturbation is altered by 180° with a change of sign of the momentum deviation, the sign of $(\beta / \beta_0 - 1)_{max}$ was chosen to be negative for a negative momentum deviation. One can see that for a small momentum deviation, both horizontal and vertical degrees of freedom exhibit approximately the same chromaticity and are linear with momentum. For large negative momentum changes, the vertical envelope chromaticity is greatly amplified which leads to the above mentioned emittance dilution.
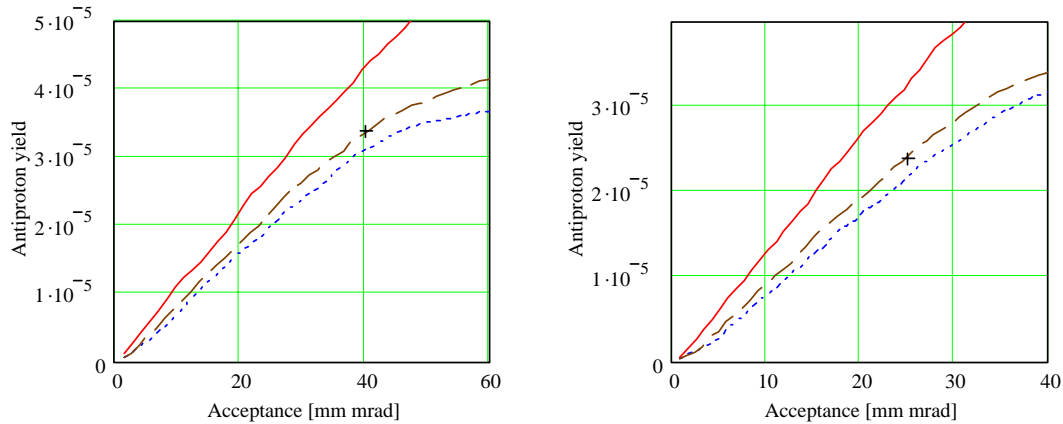
Figure 3.2.21 *Dependence of antiproton yield on acceptance for optics solutions optimized for acceptances of 25 and 40 mm mrad; solid curve – yield at the target, dashed curve – yield in the center of the transport line (Q717), dotted curve – yield at the end of the line, cross – the yield corresponding to the results presented in Figure 3.2.11.*
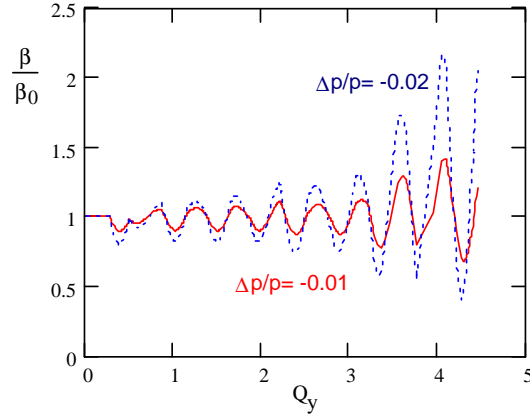
Figure 3.2.22 *Relative variations of the vertical* β *function as function of the vertical betatron phase advance for Δp/p = -0.01 (solid curve) and Δp/p = -0.02 (dotted curve).*

Although less visible in the tracking, the chromaticity of dispersion can also lead to emittance dilution. In the tracking previously described, we considered that the beam is perfectly steered through the line, resulting in the acceptance of the AP-2 line being larger than the Debuncher acceptance. In this case, there are particles on the fringe of the Debuncher acceptance. These particles are oscillating in and out due to dispersion imperfections, leaving the antiproton yield unchanged. If the acceptance of the line is the same or smaller than the Debuncher acceptance, the chromaticity of dispersion leads to an additional decrease in yield. To demonstrate the contribution of the higher order dispersion effects into beam emittance growth, Figure 3.2.24 presents the dependence of Courant-Snyder invariants excited by a momentum change for particles having zero initial betatron amplitudes. As one can see, a momentum deviation of 2% can excite the betatron motion with an effective emittance up to 2 mm mrad, corresponding to a betatron oscillation of about 25% of the machine aperture.

All of the effects described in this section can be significantly improved with a modest upgrade of the beam line optics. The change in optics may require relocating quadrupole magnets and changing power supply configurations. Additional study time will be required to formulate the upgrade path.
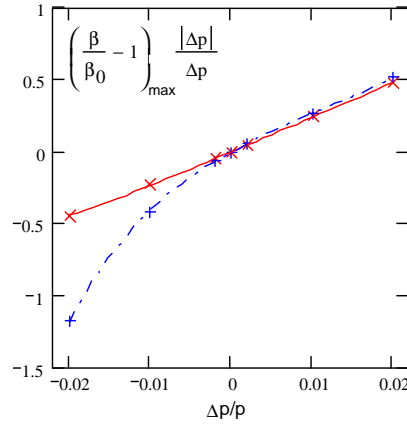
Figure 3.2.23 *Dependence of the maximum β function variation on momentum; solid curve – horizontal plane, dash-dotted curve – vertical plane.*
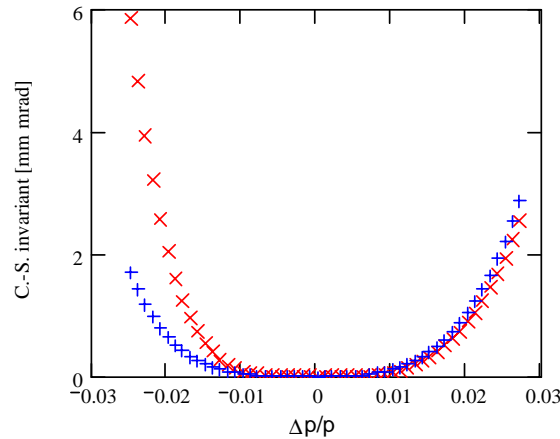
Figure 3.2.24 *Effective amplitude of betatron motion (Courant-Snyder invariant) excited in the Debuncher due to higher order dispersion;* $\times$ - *horizontal motion,* + - *vertical motion.*

3.2.2 Solid lithium lens

Efforts to create a reliable, high gradient (greater than 1000 Tesla/m with a 1 cm. lens), solid lithium conductor collection lens for Run IIb are being concentrated in three areas. First, the current lens design is being investigated to discover the nature of past failures and any predictable shortcomings of the structural design. Second, design and analysis of new lens design possibilities are being conducted with the end goal of producing and testing prototype high gradient lenses. Finally, since there are indications that the lithium pre-load pressure is important to lens survival, research and development of an improved lens filling process is underway.

3.2.2.1 Technical description

3.2.2.1.1 Current Lens Design Investigation

The existing collection lens design is being investigated in order to identify areas of improvement for future lens development. Activity is occurring on two fronts: autopsy of failed lenses and finite element analysis (FEA) of the actual design.

3.2.2.1.1.1 Autopsy of Failed Lenses

In the past, autopsy of failed lenses has been avoided due to the hazardous nature of radioactive lithium. However, with careful planning and controls in place (and since failed lenses have had appreciable time to radioactively decay), it is now safely achievable. The autopsy of the lenses will be performed by melting and removing the lithium conductor core, and then rinsing with water in order to react away any residual lithium. The work will be performed in an inert atmosphere with byproducts carefully collected and measured. After the emptied lens is disassembled, the various lens components may be visually inspected to identify locations and mechanisms of failure. Since failures have primarily consisted of breaches of the titanium cooling jacket

78

(septum) allowing lithium into the cooling water medium, it is hoped that inspection might indicate areas of the septum that require improvement.

3.2.2.1.1.2   Finite Element Analysis of Current Lens Design

FEA of the current lens design is being conducted to provide a complete visualization of the structural stresses in lens components during a pulse. The current level of FEA technology enables geometrical details and cyclic loading to be modeled that have not been included in previous analyses. The FEA of the current lens design starts with a thermal diffusion simulation of the current pulse, includes thermal and structural stress effects, and results in stress and deflection of lens components at time points of interest. All of this is done within the ANSYS FEA package. A Fermilab PPD ANSYS expert, Z. Tang, is developing this analysis method. It is hoped that results will indicate any weak points of the current lens design that can be correlated with actual lens failure autopsy results. This will greatly aid in the future design of high gradient solid lenses.

3.2.2.1.2 New High Gradient Solid Lens Design

Design efforts for a new high gradient lens are concentrated in four areas. First, a method of simulating how lens geometry changes (radius, length, end regions, etc.) affect anti-proton yield is being developed. Second, the same FEA tools described above will be utilized to evaluate new lens designs. Third, a new bonding technology (namely diffusion bonding) is being investigated for high gradient lens application. Fourth, the results of the above three areas are being applied in a prototype program that will allow real-world testing of lens design improvements.

3.2.2.1.2.1   Lens/Beam Physics Modeling

The existing design of the solid collection lens is similar to that originally conceived in the early 1980s. The lens was designed to operate with a gradient of 1000 Tesla/meter, but rather early in the target station history, it was determined that extended operation for millions of pulses is not possible above about 750 Tesla/meter. As a consequence, the collection efficiency has been less than desirable. Pbar collection is a complex, multivariable problem. Late in the 1990s, A program called MCLENS based upon the shielding code CASIM was written to model antiproton production, collection and transport. One perceived shortcoming in the MCLENS program is that the magnetic field is modeled as an infinite cylinder and does not consider end effects. This results in the overestimation of both the actual collection lens length and efficiency.

A new collection lens modeling effort based upon the MARS code was undertaken. The new model was used to generate the figures presented earlier in this section. In the MARS version of the collection lens model, non-linear, magnetic field end effects are considered. Based on the updated model, most lens parameters appear to be well optimized. One exception is the lens length. There appears to be the potential for a modest increase in antiproton yield for a lens that is approximately 20% longer. In general, though, the ideal lithium lens would be extremely short and run with a surface magnetic field far greater than present technology allows.

3.2.2.1.2.2 FEA of New Lens Designs

Using the same FEA tools developed by Z. Tang of PPD to analyze the current lens design, design improvements for the new high gradient lens will be analyzed. Effects of various materials for different components, geometrical changes, cooling parameter changes and component stresses will be investigated. As previously described, the model will simulate several cycles of loading (several hundred pulses) to achieve quasi-static status. Then stress results will be looked at from a fatigue perspective to evaluate proposed design changes.

3.2.2.1.2.3 Diffusion Bonded Septum Joints

The current method for joining individual septum components is electron beam welding. Although this method can be highly successful, it has its drawbacks in terms of fatigue, weld to weld consistency, and costs. Another method of joining (diffusion bonding) has been identified and will be investigated for applicability to septum construction. This new method of joining uses high temperature and moderate pressure to achieve complete bonding (crystal growth across joint) with more uniform microstructure, less residual stress, and for less cost than electron beam welding. Use of diffusion bonding, however, is untried for this application and requires major geometrical changes for maximum benefit. These geometrical changes can be included in the FEA mentioned earlier.

3.2.2.1.2.4 Fatigue Testing

A fatigue testing program has been undertaken in collaboration with Argonne National Laboratory's Corrosion Section. The emphasis of the testing will be to determine the endurance limit for the most critical diffusion bonded joint, located in the center of the inner conductor tube. There will also be fatigue testing of the parent material and unbonded (solid) material for comparison. To mimic actual operating loads and joint geometries, it will be necessary to utilize cylindrical joint samples and stress them in tension in the same direction as the joint line. Failed specimens will be analyzed, including microscopic evaluation, to confirm failure modes. Specimens that survive the endurance limit of $2x10^7$ cycles will be examined for cracking or other signs of imminent failure.

3.2.2.1.2.5 Prototype Program

Results of the physics modeling and FEA will be used to produce design improvements that will be tested in a series of prototype high gradient lenses. The prototypes will be constructed on an aggressive schedule in order to meet Run IIb needs. The prototypes will allow us to test pulse the new designs in a real-world operating environment. It is expected that at least two prototypes will be required before succeeding at the goal of a robust (10 million + pulses), high gradient (10+ Tesla surface field) solid collection lens.

3.2.2.1.3 Lens Filling Research and Development

Past experience and preliminary simulation results have strongly indicated that lithium pre-load pressure is linked to long term success of a solid lithium collection lens. Pre-load pressure is necessary to oppose the magnetic pinching effect during a current

pulse and keep the lithium conductor material from separating from the septum wall. Currently this pressure is provided during the initial fill of the lens with lithium. Unfortunately, because of the difficulty with volume contractions of the lithium and problems with instrumentation of the lens itself, confidence that proper pre-load pressure has been attained is not high. Research and development is currently underway to improve the fill process in terms of equipment, instrumentation, and data acquisition so that future fills of both current lenses and prototype lenses will be successful. In addition research and testing is planned to explore the possibility of adjusting the pre-load after the actual fill using, as of yet, mechanisms that are yet to be designed.

3.2.2.2 Plan and status

3.2.2.2.1 Current Lens Design Investigation

3.2.2.2.1.1   Autopsy of Failed Lenses

Five solid lenses, which have failed in service, are to be dissembled to determine the failure modes. The removal of lithium from the lenses occurs in two phases. In the first phase, a lens body is heated to the lithium melting temperature and then low-pressure argon gas is applied to aid in lithium removal. In the second phase, water is circulated through the room temperature lens body to react with and remove remaining lithium from surfaces of the steel and titanium structures. A third phase involves the recombination of hydrogen released from the second phase by controlled combustion. The collection and analysis of the resulting water vapor may shed some light on the production of gases such as helium, and hydrogen resulting from the interaction of the particle shower with lithium.

Two lenses (#20 and #21) were unfilled during the summer of 2001. Both lenses had a short service life and had failures of the inner septum. Both lenses exhibited an axial crack on the inner septum, consistent with fatigue failure. Cross-sections made at the fracture location indicate a brittle fracture propagating from the inside surface with a ductile fracture occurring over the last 1/3 of the wall thickness at the outer diameter surface. Two more lenses (#17 and #18) are being unfilled during the fall of 2001 and should have their failure analysis complete in early 2002. These lenses had a relatively long service life. The remaining lens that is scheduled for unfilling (#22) failed in September 2001 and is still very radioactive. The plan is to allow several months of cool-down time before attempting any work on this lens. Lens #22 had the longest lifetime of any lens, more than 9×10^6 pulses, and is of particular interest to us.

3.2.2.2.1.2   FEA of Current Lens Design

FEA of the current lens design is now complete. Stress and deflection results were generated for several load cases. The results have been summarized in P-Bar Note #663 "FEA Analysis of AP-0 Target Hall Collection Lens (Current Design)". In summary, stress cycles seem to be within the endurance limits of the materials. However, the analysis indicates signs of separation of lithium from the septum inner conductor tube (Ti 6Al-4V) during the magnetic pinch at the design gradient (1,000 T/m). This separation could not be modeled accurately by the ANSYS model and must be investigated further.

There is also some indication that the center body to septum seal area undergoes large deformation and/or stresses which could results in lithium leakage at the seal.

3.2.2.2.2 New High Gradient Solid Lens Design

3.2.2.2.2.1   Lens/Beam Physics Modeling

Significant progress has been made in producing the new collection lens model. Most of the programming work required for the MARS modeling work has been completed. Magnetic field calculations have been made using the program ANSYS and the results of those calculations have been incorporated in the MARS model so that end effects are now considered. Quantitative comparisons of production efficiency of the existing and future lens designs can be presently made. Since experimental data is not in complete agreement with preliminary MARS calculations, accelerator studies are planned to compare measurements with output from the model.

3.2.2.2.2.2   FEA of New Lens Designs

The ANSYS analysis of the high gradient prototype lens has been completed, although a full report has not been written. In summary, stress cycles seem to be much lower for a higher gradient (1,300 T/m). However indication of lithium/titanium separation is also apparent. Future investigations are planned to include exploration of material property temperature dependencies and the lithium/titanium separation phenomenon. However, these analyses will require careful investigations into the material properties of lithium in the plastic state (including strain rate dependencies). Projected dates for the completion of these further analyses are not easily determined. But it is hoped that a more complete understanding of the mechanical behavior of the lens during a pulse via ANSYS analyses will be achieved by spring 2002.

3.2.2.2.2.3   Diffusion Bonded Septum Joints

Diffusion bonding technology has been used to manufacture several sample joints for metallurgical analysis. From this work a joint design has been chosen as being optimal for the most critically stressed joint in the septum (inner conductor tube joint). This joint design exhibits good grain growth across the bond line, good microstructure for strength, and minimal stress concentration features (crack initiation sites) at the surface. Manufacture of the samples also resulted in the realization that, if the lens body is also made out of titanium alloy, both the body and the septum can be joined as one diffusion-bonded component. This should result in a much faster and cost effective joining process, not to mention that it eliminates a critical lithium seal. Currently 30 joint samples are being prepared for fatigue testing to determine the joint's endurance limit for fatigue.

3.2.2.2.2.4   Fatigue Testing

The diffusion bond fatigue testing program is continuing at a slow pace. All sample raw material has been prepared (bonded) and initial tensile testing of the first samples is currently underway at Argonne National Laboratory (ANL). Once sample geometry has been confirmed by these initial tests, the fatigue test samples will be final machined and sent to ANL for endurance limit determination. Past delays have been largely due to lack of test technician manpower at ANL. Future delays may involve

sample material inconsistency (more samples may need to be fabricated). Projected date for completion of the diffusion bond fatigue testing program is now spring 2002 although information regarding the endurance limit of the material may be available earlier.

3.2.2.2.2.5   Prototype Program

Time constraints have required the design of a prototype high gradient lens before all the design data have been determined (it will take several months for fatigue testing joints for instance). However, using the preliminary data currently available a reasonable first prototype can be designed and constructed that will yield valuable experience with the diffusion bonding process and indicate if identified design improvements are beneficial. This prototype is in the final stages of design. It uses a 1.5 mm titanium alloy septum wall, 1 mm was used previously. It will be constructed via diffusion bonding, which results in a water-cooled titanium alloy body. The body and septum are one piece, which eliminates the troublesome lithium seal between body and septum. It is also interesting to note that the diffusion-bonded design precludes the inclusion of lithium 'buffer' volumes that were part of the previous design.

3.2.2.2.3 Lens Filling Research and Development

The entire lens filling instrumentation system has been re-engineered to achieve better signal to noise ratio and increase sensitivity. Several tests have been run with the instrumentation system to ensure its robustness during a fill. A 'dummy' lens was assembled that made use of an actual lens assembly to mimic the fill process using hydraulic oil. Thus the fill process can be simulated many times and calibration of instrumentation at various pressures and temperatures can be performed. Compression testing of lithium has also been conducted to aid in the understanding of lithium behavior during the fill process. This information also came in useful for the lens FEA described earlier. A number of calibration runs have been performed using the dummy lens. Work on pre-load adjustment schemes has not progressed beyond the conceptual design stage.

3.2.2.2.4 Budget and manpower requirements

During FY 2002, completion of the first prototype solid lithium lens is estimated to cost 28k$ of M&S. The second prototype lens will require approximately 43k$ of M&S. Fatigue testing is estimated to incur another 45k$ of M&S. Simulation studies will require little or no outlay for M&S. Due to the research and development nature of the project, it is recommended to use a higher contingency on these projections of about 20%. Thus, the total (including contingency) M&S budget projection for FY '02 is 130 k$.

The total manpower requirement for FY '02 is 3.0 full time equivalents. The breakdown is as follows:

Physicist	@0.5 FTE
Engineer	@1.0 FTE
Technician	@0.8 FTE
Drafting	@0.7 FTE

The solid lens upgrade effort should gradually ramp down after FY '02. M&S requirements will remain about the same for FY '03 at 120 k$. For FY '04 M&S will drop

to 60k$ and then 0 k$ in FY '05. Similarly, manpower requirements will be 1.7 FTE in FY '03, dropping to 0.5 FTE in FY '04 with 0 FTE requested for FY '05.

	Total	M&S	Labor	Phys.	Eng.	Draft	Tech	CP
FY02	430	130	300	0.5	1	0.7	0.8	0
FY03	290	120	170	0.2	0.5	0.2	0.8	0
FY04	110	60	50	0.1	0.1	0	0.3	0
FY05	0	0	0	0	0	0	0	0
Project	830	310	520	0.8	1.6	0.9	1.9	0

Table 3.2.1 *Funding profile for the Solid Lithium Lens Upgrade*

3.2.3 Liquid lithium lens

3.2.3.1 Technical description

Collaboration between Fermilab and the Budker Institute of Nuclear Physics in the form of an Accord was begun in July 1997. The purpose of the Accord is to explore the feasibility of producing and operating a collection lens containing a liquid lithium conductor. It is believed that the current solid lithium collection lens operation is mainly limited due to complications arising from the rapid heating and expansion of the lithium conductor. Significant heating of the lithium conductor occurs during the electrical current pulse. In the solid lens design, large stresses develop on the titanium inner septum tube that can lead to failure. In the liquid lithium lens design, the stresses are reduced due the fluid characteristics of the liquid lithium and the use of buffer volumes. Heat deposited by the current pulse is removed by continuous pumping of the liquid lithium from the lens body to an external heat exchanger.

It is also believed that in the solid lens running at high gradient, the lithium conductor becomes separated from the inner titanium conduction tube due to a magnetic pinch, which occurs at or below design gradient. The separation of lithium from the inner conductor wall could lead to arcing in the lithium conductor, poor heat transfer, and high level cyclic stresses. In both cases, adequate pre-load pressure must be provided to prevent separation from occurring. In the liquid lithium lens, it is believed that the pressure of the lithium piping system can be controlled to prevent the separation of lithium from the inner conducting tube. The liquid lithium project as currently conceived, requires of a number of auxiliary external support systems to pump liquid lithium, control system pressure, lithium flow and lithium temperature. These systems would bring significant complications to target station operation.

3.2.3.2 Plan and status

The work outlined in the Accord is divided into four phases. Phase 1 included the performance of engineering calculations and conceptual design work. Additional design work and construction of components including a lens power supply were to be completed in Phase 2. In Phase 3, the goal is to operate a lens for 1 million pulses at a surface field of 13 Tesla. The purpose of testing a lens at such high gradient is to ensure that operation at a surface field of 10 Tesla would be reliable for many millions of pulses. In addition, the tested lens, power supply, lithium pumping and pressure systems and lens

control systems are to be delivered to Fermilab. Finally in Phase 4, a second untested lens of the same design is to be built and shipped to Fermilab.

Phases 1 and 2 are considered to be more or less complete. Phase 3 is currently ongoing. To date, two lens designs have been attempted and have failed well below the design gradient. In a review held at Fermilab during the week beginning April 9, 2001, it was learned that testing of a 3rd generation lens was scheduled to begin at BINP in May/June 2001. The testing has been delayed until at the end of 2001. It is planned to ship a lithium pumping system equipped with locking valves, pressure system, and system controls to Fermilab in the winter of 2001/2002. At the same time, a power supply designed for operation of either a solid lens or a liquid lithium lens will be shipped to Fermilab. The delivery of the tested lens will depend on completion of successful testing. The purpose of shipping the lithium contour and associated controls, perhaps in advance of delivery of a successful lens, is to get Fermilab involved in the operation of a liquid lithium system so that experience with system operation can begin to accrue.

The original Accord, which was signed in July 1997, was scheduled at that time to be completed during the year 2000. Unforeseen difficulties in this work have delayed its timely completion. At this time, an amendment is being prepared to provide additional funds to BINP to allow continued work for tasks outlined in Phase 3. Given sufficient time and resources, there is no reason to believe a liquid lithium lens can not be produced. At this time however, it is not clear that sufficient time is available to complete the liquid lens project in time for RUN IIb. If testing of a liquid lithium lens is eventually successful, significant resources will be required to configure a liquid lithium lens system into the modular form required for target vault operation.

3.2.3.3 Budget and manpower requirements

Most of the effort on the liquid lithium lens will continue to take place at BINP in FY '02. It is difficult to project the successful completion of a prototype lens, particularly in view of the lengthy delays and complications that have occurred to date. When success has been achieved, the effort will shift to Fermilab where an extensive effort will be required to adapt the liquid lithium lens to use in the pbar target vault. M&S outlay for FY '02 will be primarily for a final payment to BINP after a successful high gradient test and shipping costs associated with the lens contour and power supply.

	Total	M&S	Labor	Phys.	Eng.	Draft	Tech	CP
FY02	230	200	30	0.2	0	0	0.1	0
FY03	850	330	520	0.4	1.5	1	1.8	0.5
FY04	600	200	400	0.5	1	0.3	2	0.2
FY05	200	100	100	0.4	0.2	0	0.4	0
Project	1880	830	1050	1.5	2.7	1.3	4.3	0.7

Table 3.2.2 *Funding profile for the Liquid Lithium Lens Project*

The total manpower requirement for FY '02 is only a total of 0.3 FTE. 0.2 FTE of physicist time will be needed to monitor progress at BINP and 0.1 FTE of technician time to begin to make preparations for the arrival of the lens contour and power supply.

Anticipating a successful test in late FY '02 or early FY '03, a significant increase in M&S and labor will be required to continue the project. For instance, M&S

requirements jump to 300 k$ in FY '03 with 5.2 FTE of labor. At this point, existing target station personnel will not be adequate to cover the three Run IIb projects and operational demands. Additional engineering and technician support would be required for FY '03 and '04. Both M&S and labor are expected to drop substantially in FY '05 as the system shifts to operational use.

3.2.4 Beam sweeping

3.2.4.1 Technical description
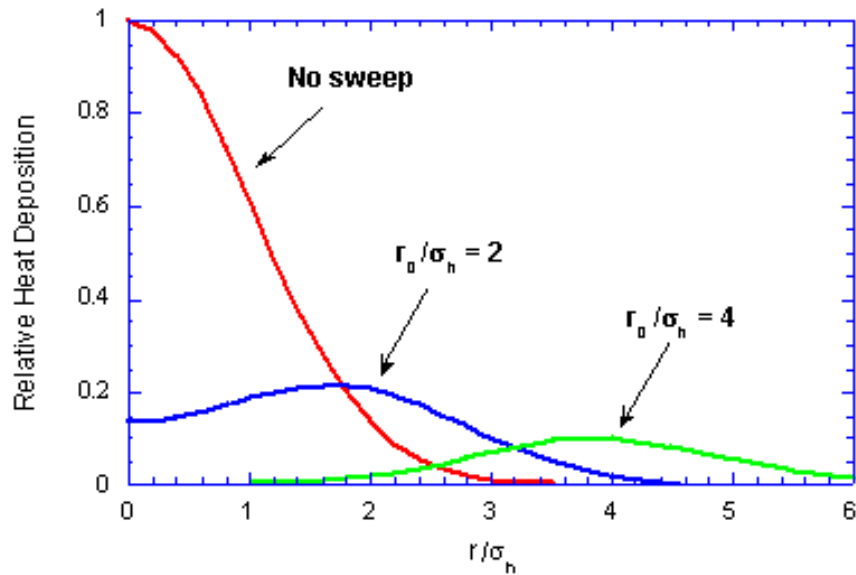
Figure 3.2.25 *Energy deposition as a function of sweep radius.*

The beam sweeping system is designed to trace a 0.33 mm radius circular pattern on the target during the beam pulse. The magnet and power supply designs evolved from this requirement and the need to provide adequate aperture for both the primary and secondary beam. Sweeping the beam 0.33 mm results in a factor of five reduction in peak energy deposition for beam with a spot size of 0.16 mm, and a factor of eight reduction with a spot size of 0.1 mm (Figure 3.2.25). This would allow targeting beam at 1×10^{13} per pulse with a spot size of 0.1 mm without damage or melting to the nickel target. As described earlier, antiproton yield is nearly maximized with a spot size of 0.1 mm.

There are two upstream magnets to sweep the beam on the target, and one magnet located immediately downstream of the collection lens to unsweep the beam. The upstream and downstream magnets are identical in design with a 2.8 cm aperture and a 56 cm length (Figure 3.2.26). Although the magnets themselves are interchangeable, the support structures and power striplines are very different. The magnets have a 2-phase, 4-conductor winding excited by two power supplies that deliver sinusoidal current waveforms in quadrature to generate a 625-kHz rotating dipole field. The field uniformity would not have been adequate without twisting the conductors by 180° over the length of the magnet. With this arrangement, the field along the beam path is uniform and rotating.

Approximately 6 kA will be required in the windings to provide a 900 G deflecting field. The peak inductive voltage drop is only 5 kV (2.5 kV to ground), reducing the risk of breakdown in the ionized environment created by the secondary beam shower. Mo-Permalloy pressed-powder cores were used because of the ease of construction and the relatively high thermal conductivity and Curie temperature of this material.

ROTATING FIELD MAGNET
LONGITUDINAL CROSS SECTION

1 – housing pipe, 2 – conductors, 3 – ceramic tube, 4 – magnet core, 5 – washer+fingerstock, 6 – end flange
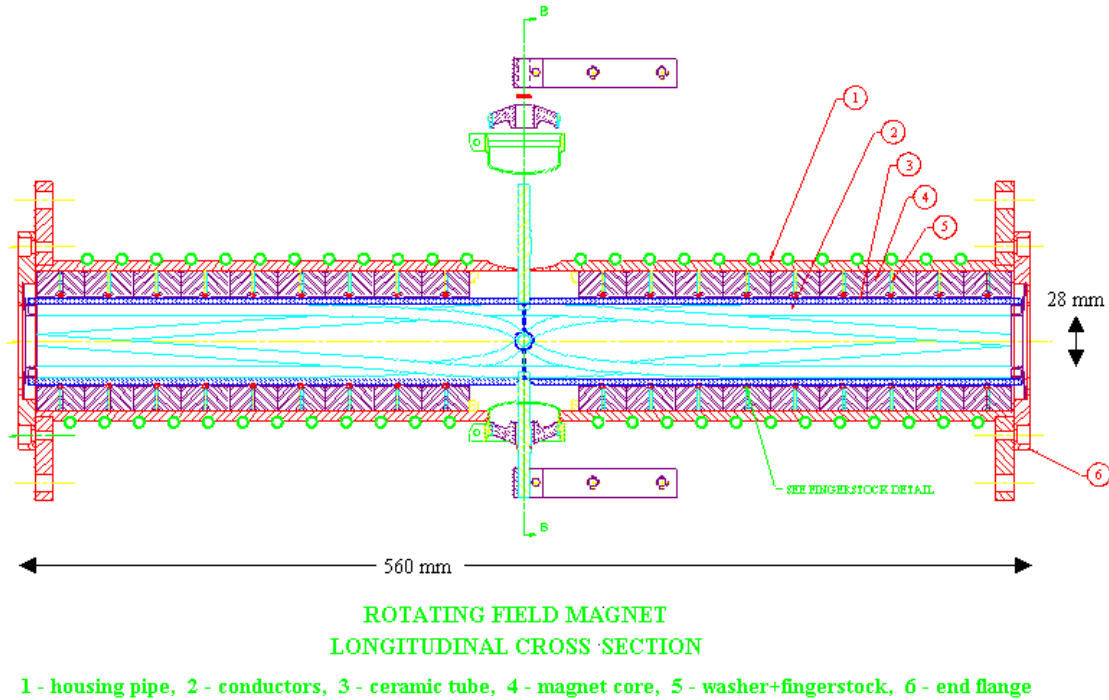
Figure 3.2.26 *Beam sweeping magnet*.

The power supplies are located on the floor of the AP-0 service building, about 15 m from \the sweeping magnets. The power supplies use pulse compression to excite a ringing circuit. Two-stage compression with saturated reactors were chosen to facilitate the transfer of the current pulse to the ringing circuit and to provide the capability to utilize a SCR switch for resonant charging of the first stage. The power supply has been somewhat over-designed and may be able to deliver up to 80% more current if a larger sweeping radius is needed in the future. The timing of the current pulse is very sensitive to component temperature, so a computer driven feedback control is required to compensate. The sweeping and unsweeping magnets also need to be precisely timed with respect to each other.

3.2.4.2 Plan and status

When the beam sweeping project was begun, it was scheduled to be completed in parallel with the construction of the Main Injector. The project is behind schedule at this point, although most of the major fabrication has been done. The sweeping magnet power supplies are essentially a custom design and many of the components were not available commercially. All of the personnel originally involved in the project have left Fermilab so there have been inefficiencies due to lack of experience.

Presently, one of the bipolar power supplies has been test pulsed approximately 2 million times. This power supply is being tested with the downstream module, stripline and magnet assembly at AP0. The two upstream sweeping power supplies have also been completed and are being tested and matched. If there aren't any major component failures during the testing phase, the power supplies will be deemed operational and tunnel installation will begin. There is also a rather complex stand-alone controls system that keeps the upstream and downstream magnet synchronized. It will be tested at AP0 with the existing test setup.

The magnets and stripline assemblies have had several design flaws that have required attention. In some cases, a total redesign has been required to make the components functional. A request was made to keep the upstream sweeping magnets under vacuum, requiring the design and fabrication of a ceramic beam pipe. A realistic goal would be to have them ready for installation in the tunnel during the winter of 2001/2002.

Despite the delays in implementing the sweeping system, it hasn't caused a serious reduction in antiproton yield yet. As the Main Injector intensity increased to 5×10^{12} ppp, there was no obvious loss of antiproton yield. The spot size on target was somewhat larger than optimal, planned lattice changes will allow a reduction in spot size. When the spot size is reduced, there will likely be local melting in the target and some loss in yield. After an initial testing program is completed with the sweeping components out of the tunnel, testing with beam will commence. Prior to installing the downstream sweeping magnet in the vault, the upstream sweeping magnets will be installed and tested with beam. The secondary emission monitor located just upstream of the target and beam position monitors in AP-2 can be used to detect beam motion. After confidence is gained in the upstream magnets, the downstream magnet can be installed and the testing phase completed. The downstream magnet will be located in an extremely radioactive environment. Once it is in place, it will be difficult to do any significant mechanical modifications due to residual radiation. The goal would be to enter the beam-testing phase in the spring 2002, with the system operational in summer 2002.

3.2.4.3 Budget and manpower requirements

The beam sweeping system is expected to be commissioned in FY '02 after lingering design problems are resolved and a testing program is completed. 50 k$ of M&S will be required to complete these tasks with 1.1 FTE of labor. The majority of the labor will be technician time for correcting design flaws and testing the equipment. The system should shift to operational use in FY '03.

	Total	M&S	Labor	Phys.	Eng.	Draft	Tech	CP
FY02	160	50	110	0.2	0.2	0	0.6	0.1
FY03	0	0	0	0	0	0	0	0
FY04	0	0	0	0	0	0	0	0
FY05	0	0	0	0	0	0	0	0
Project	160	50	110	0.2	0.2	0	0.6	0.1

Table 3.2.3 *Funding profile for beam sweeping*.

3.2.5 AP-2 and Debuncher aperture improvements

3.2.5.1 Technical description

3.2.5.1.1 Alignment

Alignment of many components is done via surveys. Beam studies can also be used to align accelerator components.

3.2.5.1.1.1   Survey

The AP-2 beamline and Debuncher ring will be surveyed as needed and when manpower is available. In particular, the sections of the accelerator that have moved due to the tunnel moving: the region where the MI-8 beamline crosses underneath the AP-2 beamline. Survey work will be done to guarantee the overall alignment of AP-1, target station and AP-2. Results of the surveys may lead us to move some elements of the accelerator.

3.2.5.1.1.2   Movable Stands

Beam studies involving the stand of a single accelerator component can be done to center the beam within the component. For some of the Debuncher elements there are stands with remotely controlled motors. A remotely controlled motor can be used to center the element while beam is circulating.

The general procedure is to heat the beam and then move an element until beam loss is observed. By finding the stand positions where beam losses begin, the component can then be centered between the loss making positions.

3.2.5.1.1.3   Portable Quadrupole Alignment Fixture

For components without motorized stands, the procedure will be to study the aperture with local bumps, make an access to move the component, and then repeat the aperture studies to see if an improvement has been made. However, moving such components requires the support of surveyors to determine the amount of the move. Due to the amount of manpower and time needed, this procedure will not be performed often.

A portable quadrupole alignment fixture has been developed. With this fixture, it is believed that the time and manpower needed would be reduced significantly for moving a quadrupole. Using this fixture, the above studies procedure could be performed quickly using only a few people (both studies and access). It is estimated that the fixture can be used on 90% of the Debuncher quadrupoles; the rest of the quadrupoles reside in areas with interfering transfer or cryogenic lines.

3.2.5.1.2 Physical Apertures

The expected beam size and aperture of components are being compared to see if there will be future restrictions as the acceptance of AP-2 and Debuncher increase. Below are the areas/elements that are currently being investigated.

3.2.5.1.2.1   Debuncher Injection Region

The AP-2 beamline injects vertically into the Debuncher ring. The injection channel has been modified recently with the replacement of the injection septum and

reorientation of a few Debuncher quadrupoles. After the injection septum, there is a BPM-quadrupole combination. The BPM and star-chamber beam pipe through the quadrupole are special larger aperture versions of these types of components and have been offset vertically during the recent work. A picture looking down the vacuum chamber (taken during the installation of the new injection septum) shows that the top of the BPM appears to be lower than the wall of the upper part of the star-chamber. The vertically injected beam may be hitting the top of the BPM. Even with moving the BPM, the quadrupole could still be an aperture for greater than 35 mm-mrad injected beam.

The current SQC quadrupole can be replaced with a LQD quadrupole. The LQD pole-to-pole distance is nearly the same diameter of the extended star-chamber inside of the SQC; a large star-chamber made to fit within a LQD will have plenty of aperture. The Debuncher dipole bus and a 200A power supply could power the LQD to achieve the same field strength as the current SQC. The BPM can be placed on the downstream side of the quadrupole.

3.2.5.1.2.2 RF Cavities

Three RF cavities are located in regions of high dispersion in the Debuncher. With larger acceptance, the increased beam size combined with dispersion may cause DRF1-1, DRF2 and DRF3 to become aperture restrictions. DRF1-1 and DRF2 are located in the same lattice locations (D=1m) while DRF3 resides where the dispersion is 1.6m. The smaller DRF2 and DRF3 cavities are located in the first region of dispersion after injection. Relocating the cavities to low dispersion regions (~0m) would remove the dispersion contribution to the beam size through these cavities.

3.2.5.1.2.3 Debuncher Cooling Band 4

The separation of the arrays in the band 4 tanks of the Debuncher cooling system is 38.1 mm. For the upstream ends of the horizontal band 4 tanks, β_h is 9.2 m. β_v is 11.2 m at the upstream end of the vertical band 4 tank. With the current arrays, the β functions would have to be less than 9.1 m to achieve 40 mm mrad. The current tanks provide horizontal and vertical apertures of 38.4 mm mrad and 32.4 mm mrad, respectively.

3.2.5.1.2.4 Dipole Beam Pipes

The beam pipe within the dipoles of AP-2 and the Debuncher are not curved. In some cases, the dipoles themselves are not curved: modified wide-gap B1 magnets and four 6-4-120 magnets in AP-2. A straight magnet is oriented to be parallel to the orbit in the middle of the magnet and offset so that the beam's curved orbit does not hit the vacuum chamber wall. The other dipoles, two wide-gap SDE magnets in the AP-2 and all of the Debuncher SDD magnets, are curved but the vacuum chamber is made up of two straight rectangular pipes welded at an angle.

3.2.5.1.3 Orbit Correction

Improved orbit control will make it easier to avoid aperture obstructions. Due to the Debuncher cooling upgrades, many trim dipoles were removed and there is not much real estate to apply trims in new locations.

3.2.5.1.3.1 AP-2

Currently, AP-2 steering is done with a total of nine trim dipoles spread throughout the beamline. Changes in any of the trim dipoles affect the entire orbit; additional steering is required. The decommissioned Debuncher trim dipoles and power supplies can be applied to the AP-2 beamline. The only new items will be stands for the trim dipoles (the AP2 beamline hangs from the enclosure ceiling) and cable runs. Also individual shunts on the major left bend (six dipoles) will be installed to provide steering.

3.2.5.1.3.2   Debuncher

There are few places in the Debuncher where trim dipoles can be inserted. Due to this space limitation, remotely controlled Debuncher quadrupole stands will be used to induce dipole kicks. One advantage of movable stands is that kicks in both planes can be implemented.

3.2.5.1.4 BPM Systems

The BPM systems of AP-2 and the Debuncher are based upon a Z80 processor data acquisition. The knowledge to keep these electronics functioning is limited and the Debuncher BPM system with its multiplexer switch and gain system make the BPM systems not very reliable and hard to maintain. Parts of the BPM electronics and data acquisition system will be replaced.

3.2.5.1.4.1   AP-2

The AM/PM RF modules of the AP-2 BPM system will be retained while new sample-hold electronics and a commercial data acquisition will be implemented. The data acquisition will communicate with an ACNET front end via Ethernet. All changes are done upstairs in the service building; no accesses will be necessary for implementation.
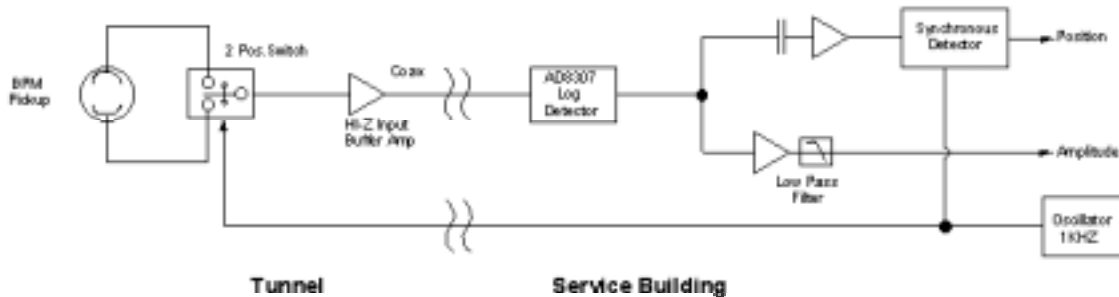
Figure 3.2.27 *BPM system*

During reverse proton studies of the AP-2 line, it is desirable to have the beam position measured between quadrupoles IQ1-4 and the lithium lens. A BPM assembly could be installed in an available slot in the target vault to provide beam positions in both planes.

3.2.5.1.4.2   Debuncher

The current Debuncher BPM system was designed to be used in a closed orbit mode (2.5MHz) and a turn-by-turn mode (53MHz). Historically, the latter mode has not been used much. The new BPM systems will be specialized to perform closed orbit

measurements. The Debuncher BPM system consists of 120 beam pickups. The signals are routed to six "houses". Each house handles 20 channels of BPM data.

Generally signals from each of the pickups, here referred to as A and B, are combined in hardware to give sum and difference signals or are brought individually to the electronics for further processing. Matching the signal paths and calibrating out the differences can be costly. This design attempts to alleviate some of the problems by using only one RF signal path and switching between A and B signals.

A solid state RF switch is positioned as close to A and B pickup outputs as practical. This minimizes the length of the connecting line and allows for easier gain matching. The output of the RF switch is routed up to the service building where the rest of the electronics are located. The RF signal is received by a logarithmic amplifier whose output is proportional to the log of the amplitude of the received signal. Rapidly alternating the RF switch between A and B channels produces an amplitude modulated signal. This amplitude modulation is proportional to the amplitude difference between A and B pickups and appears at the output of the log amp as square wave modulation riding on the average signal level. A synchronous detector, implemented either by an op-amp circuit whose gain is switched between +1 and -1 or by subtracting alternating samples from an A/D converter, is used to recover the amplitude of the modulated signal. Synchronous detection is a very powerful method of signal recovery.

The tunnel electronics consisting of protection diodes, solid state switch, buffer amplifiers, calibration coupler and regulators are contained in a connectorized box similar to the one used in the Accumulator BPM's. The switch is operated by a buffered TTL signal from the service building electronics. The beam is bunched by an existing 2.5 MHz RF system. An Analog Devices AD8307 Log Detector receives the amplitude modulated 2.5 MHz signal. The dynamic range is -60 dBm to +12 dBm. The output of the log detector can either be synchronously demodulated by an Analog Devices AD630 or sent to an A/D converter and demodulated in software. Hardware demodulation has the disadvantage of requiring individual alignment of each channel. A test unit uses a standard 200 MHz Pentium desktop computer with a National Instruments PCI-6032E 16 channel, 16 bit, 100 ksample/sec converter card. A PC104 format processor and A/D card will be tested soon. Approximately 80,000 floating point operations per second are required to digitally process the data for each house. Once processed, the intensity and position data will probably only need to be updated at 15 Hz or slower. The house processors will communicate with an ACNET front-end processor via Ethernet. The front end will format the data streams for presentation to the standard ACNET Console and provide for further data processing and presentation. A simple TCP/IP protocol has been demonstrated to work between the house processor and the front end.

3.2.5.1.5 Debuncher Lattice

Improved AP-2 and Debuncher apertures will allow beam to be spread out over a greater phase space than what has been handled by the Debuncher before. It is not apparent that the Debuncher is capable of performing all the necessary functions to the beam in additional phase space. Studies of the Debuncher will be done to determine if there is any need for lattice upgrades.Three possible lattice improvements are being considered to ensure that the dynamic aperture exceeds the physical aperture and optimizing the lattice for both RF bunch rotation and stochastic cooling. There is no

provision in the Debuncher for skew-quadrupole errors, which could further increase the beam size and cause the beam to be scraped; skew-quad correctors may be needed. The Debuncher operates with a tune near 9.75 in both planes; it is not known if beam in the additional phase space will interact with either fourth order resonance and require octupole correctors. A γ_t ramp may be desirable to provide a sufficiently large RF bucket for bunch rotation (small value of η increasing the momentum aperture at injection) and sufficient mixing for stochastic cooling (large value of η).

3.2.5.2 Plan and status

3.2.5.2.1 Alignment

3.2.5.2.1.1   Survey

The Antiproton Source has a standing request to perform surveys when the resources are available. Hopefully over the next year, the surveying requirements for the rest of Fermilab will allow the surveying of AP-1, target station, AP-2 and Debuncher.

On occasion, quick surveys of suspect single components have been. During the Fall 2001 shutdown, the DRF2 and DRF3 cavity tanks showed elevated levels of radioactive activation to the inside (of the Debuncher ring).   Mis-alignment was considered with other possibilities for the explanation of the activation (decay products after the first dipole in the Debuncher, mis-steering of the beam and first aperture restriction in the Debuncher). Surveyors found both ends of each tanks off the centerline defined by the surrounding quadrupoles; the tanks have been aligned. As studies and measurements indicate, surveys and alignment of specific components will be done.

3.2.5.2.1.2   Movable Stands

Most of the Debuncher pick-ups and kickers are movable. These stands have been, and will continued to be, exercised to center the component on the beam. At this time, the only plans for adding new movable stands is for quadrupoles to be used for beam steering (see below).

3.2.5.2.1.3   Portable Quadrupole Alignment Fixture

An early prototype for the alignment stand is currently being worked on. Some engineering work still needs to be done to mount the necessary measurement calipers to the device. High accuracy digital calipers have already been procured. The fixture should be completed and ready for lab testing early 2002. To use the fixture in the tunnel will require frequent access interspersed with beam studies to position the quadrupole; this procedure is expected to take 1-2 shifts per quadrupole. .

3.2.5.2.2 Physical Apertures

3.2.5.2.2.1   Debuncher Injection Region

The LQD magnets are used in one place of the Accumulator lattice (6 total). Currently, there is only one spare LQD. The option to build another LQD is being investigated. If the existing LQD is inserted, the SQC with the modified star-chamber will be left in the tunnel ready for easy re-insertion if the LQD is needed in the

Accumulator. A special beam pipe for the LQD needs to be made and new bellow-flange units will have to be designed and fabricated.

3.2.5.2.2.2   RF Cavities

Three DRF3 options that have been proposed:

Option 1) Move DRF3 upstream by 34". It will require no cabling work, just vacuum. Since D' between D5Q10 and D5Q11 is non-zero, the closer to D5Q10, the better. This move reduces dispersion from 1.6 M to ~1.4 M.

Option 2) Move DRF3 from its present position between D5Q10 and D5Q11 to the upstream end of D5Q10. This will require IP510 (ion pump) be moved to the downstream end of D5Q10, and DRF2 moved upstream to make enough room. Again, no cabling work is necessary, but vacuum work and welding will be. A bellows will need to be added between the cavities. The dispersion at DRF3 then goes from 1.6 M down to 1.05 M. This looks like a best first thing to try.

Option 3) DRF3 can be relocated to the downstream end of the adiabatic cavity DRF1-8 (between D5Q6 and D5Q7). Dispersion here is –0.002 M. To make this work, DRF1-8 will need to be moved upstream by 18" and have 3" of beam pipe trimmed off each end. IP506 will need to be moved to the upstream end of D5Q6. Also, the RF phase for DRF1-8 would need to be changed (cabling upstairs) and the fan-back cable shortened to compensate for the reduced time of flight between cavities. Bellows between cavities and a spool piece to replace DRF3 at its old location will be needed. This move is nice because if we do decide to move any other RF in the Debuncher, the DRF3 cavity will not need to be relocated again.

 Unfortunately, moving DRF2 or DRF1-1 is considerably more involved. However, it is possible to put every one of the RF cavities in a region of low dispersion.

1) Remove both DRF2 and DRF3 from their present positions and replace the sections with large aperture spool pieces. Install both cavities between D5Q6 and D5Q7 where DRF1-8 presently is. This will not require any upstairs changes, just re-routing DRF2 and DRF3 cables.

2) For the adiabatic cavities, remove DRF1-1 and DRF1-8 from the beamline and move them both over to D20. At present, there is room between D2Q7 and D2Q6 for DRF1-1 if the horizontal and vertical trim dipoles are removed and a movable quad stand is placed under either of these two quads. DRF1-8 could be installed between D2Q6 and D2Q5 if the pump-out port and ion pump are moved to one end of the straight.

3) The issues concerning controls for the adiabatic cavities are much more involved. Presently, there is enough room in AP30 to house all of the amplifiers and low level equipment. There is also the matter of bringing the necessary RF signals in for system drive and phase lock.

3.2.5.2.2.3   Debuncher Cooling Band 4

The Debuncher cooling band 4 arrays would have to be redesigned so that the separation of the arrays is at least 42.3 mm to achieve 40 mm mrad aperture. Other choices include decreasing the beta functions through the tanks or removing band 4 cooling. Studies will be performed to determine the effect of removing band 4 from the overall cooling system.

3.2.5.2.2.4   Dipole Beam Pipes

Simulations will be performed to determine if any of the dipole vacuum chambers need to be replaced. New beam pipes will have to be designed and installation will require significant downtime. This is work that would not be done in the next few years.

3.2.5.2.3 Orbit Correction

3.2.5.2.3.1   AP-2

The elements of AP-2 are well separated with the exception of components at the upstream end (prior to quadrupole Q704), in the major left bend (between Q716 and Q721) and at the downstream end (Q730 to the injection septum).

Forward proton studies (requiring the polarity to the AP-2 beamline and Debuncher to be switched) done in February 2001 showed a *bouncing* horizontal orbit during the first long straight section. The horizontal bend elements at the upstream end of AP-2 are the momentum selecting magnet (PMAG) within the target station and a short left bend dipole H704; the first horizontal trim dipole is after Q711: HT711. The phase advance between PMAG and H704 is nearly 180°. The distance between Q704 and H704 is 6m. A horizontal trim dipole (proposed HT704) placed directly downstream of quad 704 would be 90° from both PMAG and H704.

Vertical orbit correction at the upstream end of the AP-2 beamline is done by two trim dipoles: VT702 and VT706. These trims are not optimally situated since the phase advance between them is 135°. If a new trim dipole (proposed VT704) is added near H704, then the phase advance from VT702 will be 90°. Unfortunately, the current vertical beta function passes through a minimum (4 meters) at H704.

At the down stream end of AP-2, one needs to be concerned about the position and angle to the entrance of the injection septum. In the horizontal plane, HT730 and HT731 are ideally situated at respectively 180° and 90° in phase advance from the injection septum. Vertically, the only control is the downward bend dipole V730, which is phase advance 360° prior to the entrance to the injection septum. Another vertical correction device is desired. At 90° prior to the injection septum is Q732 in a well-packed region. Further upstream, VT730 could be inserted directly after HT730 and would be nearly at the correct phase advance. Otherwise, one would need to go to 450° in phase: just prior to Q727 and 48m from the injection septum. Proposed VT727 is desirable anyway for position control at V730. The difficulty with inserting VT730 is that the beam line is headed downward and essentially above the Debuncher. Whereas the other correction dipoles will be a relatively straightforward installation, VT730 will be more difficult due to its location and orientation.

During the Fall 2001 shutdown, shunts have been added to six dipole magnets providing horizontal control through the major left bend. If vertical control is deemed necessary through the bending section, then there is plenty of room to insert dipole trims.

Due to limited manpower, none of the dipole trims have been installed. It will probably take two shutdown days to install a stand, dipole trim and cables per location; the exception is the proposed VT730.

3.2.5.2.3.2   Debuncher

For the last year, five motorized stands have been used in the Debuncher. In both planes, local bumps have been successfully implemented by using a combination of these movable quads and existing trim dipoles. Ten more of these stands (9 SQC and 1 SQD style) were constructed this last summer and the flexible bellows have been ordered. These will be installed in the first half of 2002 when manpower and shutdowns permits (several days). The injection, extraction and cooling system pickup regions are the priority. To have a complete set of local orbit bumps, an additional twenty motorized quadrupole stands will be needed. Beam studies will help define where further motorized stands will be needed for orbit control.

3.2.5.2.4 BPM Systems

3.2.5.2.4.1   AP-2

CDF collaborator Alexei Semenov designed a new sample-hold unit during 2001. Five prototype boards have been fabricated; final assembly of the board and testing need to be done. A few commercial available WebDAQ units have been purchased. Brian Winer and Richard Hughes of Ohio State University (CDF) along with Beams Division Controls Department have shown that java programs can communicate with the WebDAQ within the ACNET environment. Clock-trigger cables will have to be pulled to each house location. In 2002, testing will be done by installing a house in parallel with the existing system in AP50. To implement along the entire AP-2 beamline, the F27 service building needs to have Ethernet installed.

There are presently no BPM's located in the target vault. It would be desirable to have at least one BPM in each plane in the vault to improve orbit measurements of AP-2 made with reverse protons. A new BPM assembly will need to be fabricated and adapted for use in the target vault. Support electronics will also be required as there are presently none in the AP-0 service building.

3.2.5.2.4.2   Debuncher

Using a Stanford Research model DS345 Function Generator as a modulated signal source and a Tektronix TDS3012 oscilloscope as the synchronous detector, modulation of 0.02 dB can be clearly detected. A signal with no modulation results in an equivalent noise floor of 0.002 dB. Figure 3.2.28 shows the test setup used to characterize the performance of the log amp and data acquisition system. With a 3 dB difference between A and B signals, the worst-case (when not calibrated) error was 0.16 dB. Calibration reduced the worst-case error to 0.05 dB. The average deviation was 0.0095 dB. On a test stand, an Accumulator style split sleeve BPM pickup has been investigated. Scaling to the larger Debuncher BPM pickup, the central sensitivity between 2.5 MHz and 53 MHz is 0.373 dB/mm. Plate to plate isolation is 40 dB at 2.5 MHz.

In FY2001, Fermilab Record of Invention FAA-783 was submitted. Demonstration of performance of synchronous detection has been shown. Printed circuit

cards have been fabricated for the pickup switching and buffer electronics as well as for the log detector and synchronous demodulator electronics. Data acquisition using a 16 channel 16 bit PCI A/D converter card was shown to work in a modest desktop PC. A java based Open Access Client (OAC) was demonstrated for transferring measurement data from a PC to ACNET.
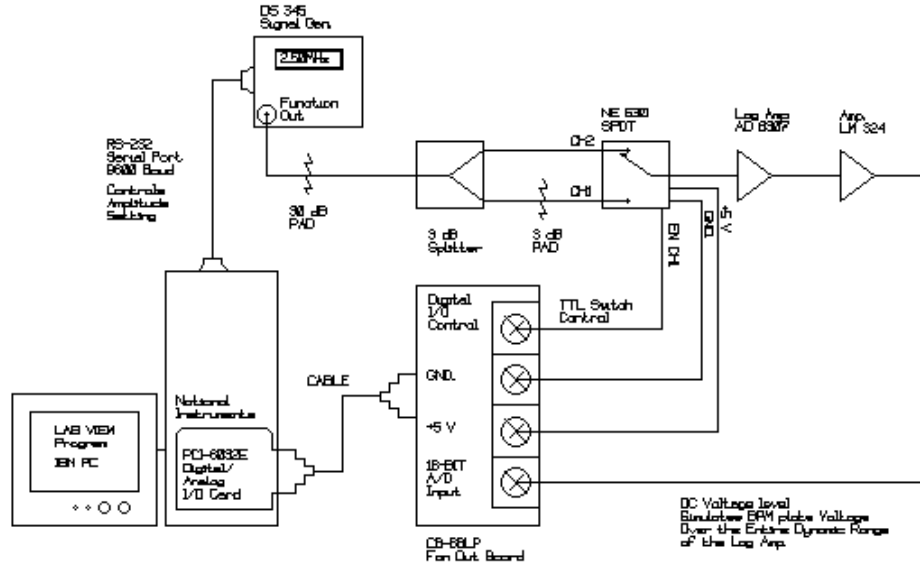

Figure 3.2.28 *BPM system*

Bench testing of the switching preamp will be conducted at the beginning of FY2002. Additional measurements of the full aperture response of a split plate BPM pickup will be done to fully characterize the non-linearities. A PC-104 industrial computer will be tested for data acquisition and demodulation. Additional work will begin be done on the OAC to communicate with small processors using standard TCP/IP requests.

A beam test using the synchronous demodulation scheme on a single BPM will be done early in 2002. It is expected that a full (20 BPM) house will be ready for testing in the spring of 2002; installation will depend upon the availability of tunnel time. Installation of all 120 preamps in the tunnel could be completed by fall 2002. Early in FY2003, the installation of service building electronics and commissioning of the system and application software will be done.

3.2.5.2.5 *Debuncher Lattice*

The Debuncher lattice model is being upgraded and studies will be performed to verify the lattice model. Further studies and modeling will be done to investigate possible problems with the larger beam phase space in the Debuncher. The results of the studies and modeling will determine if any upgrades are needed.

3.2.5.3 Budget and manpower requirements

Most of the projections are "top-down" due to the nature of not knowing the results of studies or simulations. The estimates assume that all projects are necessary. The

projections given below present labor in the following format: Phys./ Eng./ Tech./ Draft./ Comp. Prof. FTEs.

3.2.5.3.1 Alignment

Alignment will be ongoing project. In FY02, the portable quadrupole alignment fixture will be finished. The FY02 cost is 50 k$ and labor is 0.2/0.0/0.2/0.0/0.0. The estimates for FY03-FY05 are 25 k$ and 0.2/0.0/0.1/0.0/0.0.

	Total	M&S	Labor	Phys.	Eng.	Draft	Tech	CP
FY02	90	50	40	0.2	0	0	0.2	0
FY03	55	25	30	0.2	0	0	0.1	0
FY04	55	25	30	0.2	0	0	0.1	0
FY05	55	25	30	0.2	0	0	0.1	0
Project	255	125	130	0.8	0	0	0.5	0

Table 3.2.4 *Funding profile for aperture alignment.*

3.2.5.3.2 Physical Apertures

Studies in FY02 will define the path for the following years. Projects will start in FY02 with costs and labor of 200 k$ and 0.3/0.2/0.2/0.2/0.0. The main project years will be FY03 and FY04; each will incur costs and labor requirements of 600 k$ and 0.3/0.5/2.0/1.0/0.0. The projects will be finish in FY05: 250 k$ and 0.3/0.2/1.0/0.2/0.0.

	Total	M&S	Labor	Phys.	Eng.	Draft	Tech	CP
FY02	290	200	90	0.3	0.2	0.2	0.2	0
FY03	980	600	380	0.3	0.5	1	2	0
FY04	980	600	380	0.3	0.5	1	2	0
FY05	330	250	80	0.3	0.2	0.2	0.1	0
Project	2580	1650	930	1.2	1.4	2.4	4.3	0

Table 3.2.5 *Funding profile for physical aperture project.*

3.2.5.3.3 Orbit Control

Most of the orbit control will be done during the FY02 and FY03; each will be 200 k$ and 0.5/0.1/0.2/0.2/0.2. The final two years, FY04 and FY05, will be to do fine tuning of the orbit control: each 75 k$ and 0.2/0.0/0.1/0.1/0.0.

	Total	M&S	Labor	Phys.	Eng.	Draft	Tech	CP
FY02	320	200	120	0.5	0.1	0.2	0.2	0.2
FY03	320	200	120	0.5	0.1	0.2	0.2	0.2
FY04	115	75	40	0.2	0	0.1	0.1	0
FY05	115	75	40	0.2	0	0.1	0.1	0
Project	870	550	320	1.4	0.2	0.6	0.6	0.4

Table 3.2.6 *Funding profile for orbit control project*

3.2.5.3.4 BPM Systems

The goal is to get both systems operational as soon as possible to help with the studies. It is expected that the work can be completed in FY02 and FY03; each will cost 100 k$ and the labor will be 0.2/1.5/2.0/0.0/1.0.

	Total	M&S	Labor	Phys.	Eng.	Draft	Tech	CP
FY02	570	100	470	0.2	1.5	0	2	1
FY03	570	100	470	0.2	1.5	0	2	1
FY04	0	0	0	0	0	0	0	0
FY05	0	0	0	0	0	0	0	0
Project	1140	200	940	0.4	3	0	4	2

Table 3.2.7 *Funding profile for BPM systems project*

3.2.5.3.5 Debuncher Lattice

In FY02, studies and initial designs will be done incurring no cost, 0 k$; labor will be 1.0/0.2/0.1/0.1/0.0. The projects will mainly be done in FY03 and FY04 each incurring cost of 500 k$ and using labor of 1.0/1.0/2.0/0.8/0.5. The projects should finish in FY05: 200 k$ and 0.5/0.2/1.0/0.2/0.5.

	Total	M&S	Labor	Phys.	Eng.	Draft	Tech	CP
FY02	140	0	140	1	0.2	0.1	0.1	0
FY03	1030	500	530	1	1	0.8	2	0.5
FY04	1030	500	530	1	1	0.8	2	0.5
FY05	440	200	240	0.5	0.2	0.2	1	0.5
Project	2640	1200	1440	3.5	2.4	1.9	5.1	1.5

Table 3.2.8 *Funding Profile for Debuncher lattice upgrade*.

3.2.6 Conclusion

By implementing the upgrades suggested in this section, antiproton yield in the Debuncher could approach 40×10^{-6} antiprotons per proton. After examining the physics principles involved in targeting and collecting beam, it is clear that increasing the aperture of AP-2 and the Debuncher is the surest way to increase antiproton production efficiency into the Debuncher. Increasing the number of protons on the production target with Main Injector slip-stacking is described in another section, it will bring a nearly linear increase in antiproton flux into the Debuncher. The challenge with slip-stacking from the perspective of the antiproton source is to maintain the same production efficiency from the target station with increased heating of the target. The beam sweeping system should be able to accomplish this goal and should be operational before the Main Injector intensity is increased.
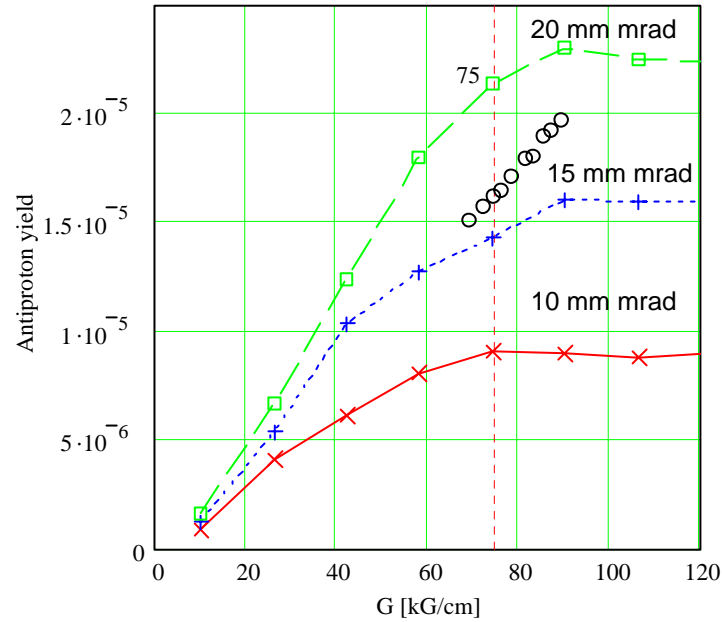
Figure 3.2.29 *Modeled lens gradient vs. yield with experimental data.*

Considerable effort has been put into increasing the gradient of the lithium lens while preserving a reasonable operational lifetime. The motivation for increasing the lens gradient has been based on measurements made during Collider Run I. The measurements suggested that a nearly linear relationship existed between antiproton production efficiency into the Debuncher and lithium lens gradient. Figure 3.2.29 has data from one of these studies overlaying data generated from the beam model. As our understanding of the antiproton production and collection process improves, so too does the realization that beam spot size, target length, lithium lens strength, the AP-2 lattice and AP-2 and Debuncher apertures are all intertwined in a complex fashion. It is difficult to only change one or two of these parameters in a beam study and generate meaningful results.

Carefully planned and executed beam studies will be crucial in improving our understanding of the present state of the antiproton source and accurately identifying improvements. Measurements of the AP-2 lattice are particularly important for understanding the dynamic aperture of that line and confirming that beam entering the Debuncher is properly matched. Measurements of the relationship between beam spot size on the production target and AP-2 and Debuncher yield can be compared to the model to estimate apertures at various points. For the proposed upgrades to succeed, adequate study time must be provided during Run IIa.